

Simulation of in-plane vibrations of 2D structural solids with singularities using an efficient wave based prediction technique

Caroline Vanmaele^{1,2}, Karel Vergote^{1,3}, Dirk Vandepitte¹,
Wim Desmet¹

¹ *KU Leuven, Department of Mechanical Engineering
Celestijnenlaan 300 B, B-3001, Heverlee, Belgium*

² *Atlas Copco Airpower NV – Airtec
Boomsesteenweg 957, 2610 Wilrijk, Belgium*

³ *Bosal ECS
Dellestraat 20, B-3560 Lummen, Belgium
e-mail: karel.vergote@gmail.com*

This paper proposes the wave based method for the steady-state dynamic analysis of the in-plane behaviour of 2D structural solids. This novel prediction technique relaxes the frequency limitations of the commonly used finite element method through an improved computational efficiency. This efficiency is obtained by selecting basis functions which satisfy the governing equations *a priori*, in accordance with the indirect Trefftz approach. Special attention is paid to problems in which singularities appear in the problem solution. For these problems, the conventional set of basis functions is extended with functions which can represent the singularity accurately. The capabilities of this novel method for mid-frequency applications, as compared to the standard finite element method, are demonstrated by means of two numerical examples.

Keywords: structural dynamics, wave based method, indirect Trefftz method, plate membrane, stress singularities, corner functions.

1. INTRODUCTION

Nowadays, the finite element method (FEM) is the most widespread technique for the steady-state dynamic analysis of structural components [4, 40]. The FEM is based on the discretisation of the considered structure into small elemental domains. Within each element, the dynamic field variables are expressed in terms of local, predefined and usually polynomial shape functions, which satisfy only the Dirichlet boundary conditions and which do not fulfil the governing differential equations. The solution is determined by restoring the differential relations and Neumann boundary conditions in an integral sense. Due to the approximative nature of the shape functions, the number of elements and the subsequent size of the models increase with increasing frequency, such that the use of the FEM is practically limited to low-frequency applications. An additional disadvantage of the polynomial nature of the shape functions is that it is difficult to obtain reliable results when the strains or stresses become singular due to a large pollution error invading the whole domain [21, 26]. In order to acquire acceptable results, the mesh should be refined in the vicinity of the singularity.

An alternative group of deterministic simulation techniques are the so-called Trefftz-based methods, such as the variational theory of complex rays [6, 18], the method of fundamental solutions [13] and the wave based method (WBM) [12]. Those methods are based on the Trefftz principle [32] in the fact that the field variables are expressed in terms of functions which satisfy the governing equations *a priori*. The WBM, which is the topic of this paper, relaxes the frequency limitation of the FEM through an enhanced computational efficiency. It starts by partitioning the problem

domain into a small number of large, convex subdomains. The convexity of the subdomains is a sufficient condition for the convergence of the WBM. Since the field variables are expressed in terms of an expansion of wave functions which satisfy the governing equations *a priori*, there is only an approximation error introduced on the boundary and interface conditions for each subdomain. The minimisation of this approximation error leads to a system of equations which can be solved for the unknown contribution factor of each wave function. Since no fine domain discretisation is required, the model matrices of the WBM are substantially smaller than those of the FEM. Thanks to the smaller model matrices and the subsequent smaller computational load, the application of the WBM can be extended towards higher frequencies as compared to the FEM. Previous validations showed the capabilities of the WBM for interior and exterior (vibro-) acoustic problems [5, 22–24, 33, 37, 38], for dynamic plate bending problems [34] and for poro-elastic problems [9].

This paper proposes the development of the WBM for the simulation of the in-plane behaviour of 2D structural solids, also known as the “membrane behaviour” of flat plates. Specific attention is paid to the presence of singularities in the vicinity of corner points. Such singularities can lead to convergence problems for the WBM. For plate bending and poro-elasticity, these convergence problems are solved by including some special purpose functions, termed ‘corner functions’, in the expansion set [8, 35]. The only purpose of the corner functions is to provide an accurate representation of the singular behaviour of the problem solution in the vicinity of the corner point. A similar methodology will be applied for the dynamic in-plane 2D structural solid problems considered in this paper. Jirousek discussed the use of special purpose functions for stress singularities in the hybrid Trefftz FEM for static in-plane plate problems [15]. Sinclair gives an extensive overview of the different types of singularities which can occur in static in-plane problems [28], including a discussion of possible corner functions. For dynamic problems, the use of corner functions has mainly been restricted to plate bending problems. Leissa and Huang presented a procedure based on a Ritz method where the conventional set of basis functions is extended with corner functions of the associated static problem [16, 19]. Similar to this principle, this paper uses dynamic corner functions, derived from the associated static problem, to extend the set of basis functions.

The paper starts with the definition of the general 2D structural in-plane problem. The next section discusses the singularities which can occur. An asymptotic analysis leads to an understanding of the possible singular fields. In addition, it allows to define some functions which asymptotically represent the strain and stress fields. These functions can be used as corner functions in the WBM. Subsequently, the basic principles of the WBM are explained. Finally, the use of the WBM is demonstrated for two numerical examples. Both examples indicate the beneficial convergence rate of the WBM as compared to the FEM. Furthermore, it is confirmed that the corner functions are essential for the accuracy of the WBM.

2. PROBLEM DEFINITION

A problem definition is given in Fig. 1. The in-plane displacements w_x and w_y at any position (x, y) on the mid-plane of the plate domain Ω_s can be described by the coupled dynamic Navier equations:

$$\begin{aligned} \frac{\partial^2 w_x}{\partial x^2} + \frac{1-\nu}{2} \frac{\partial^2 w_x}{\partial y^2} + \frac{1+\nu}{2} \frac{\partial^2 w_y}{\partial x \partial y} + \frac{\rho(1-\nu^2)\omega^2}{E} w_x &= 0, \\ \frac{\partial^2 w_y}{\partial y^2} + \frac{1-\nu}{2} \frac{\partial^2 w_y}{\partial x^2} + \frac{1+\nu}{2} \frac{\partial^2 w_x}{\partial x \partial y} + \frac{\rho(1-\nu^2)\omega^2}{E} w_y &= 0 \end{aligned} \tag{1}$$

with E the elasticity modulus, ν the Poisson coefficient, ρ the material density. The FEM makes use of the coupled Navier equations to derive the model matrices. The WBM, on the other hand, makes use of exact analytical solutions of the homogeneous equations to define the basis functions. In order

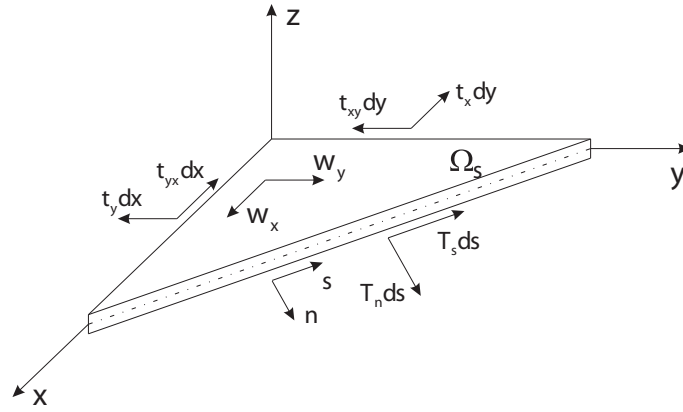


Fig. 1. In-plane forces acting on a plate section.

to simplify the solution of these equations, the Navier equations are transformed into two uncoupled equations. The considered transformation decomposes the displacement field in a dilatational and rotational strain [2]:

$$\begin{cases} w_x \\ w_y \end{cases} = -\frac{1}{k_l^2} \nabla e + \frac{1}{k_t^2} \nabla \times \Omega, \quad (2)$$

with e and Ω the dilatational and rotational strain. By means of this transformation, the coupled equations are transformed in the following uncoupled equations:

$$\begin{aligned} \nabla^2 e + k_l^2 e &= 0, \\ \nabla^2 \Omega + k_t^2 \Omega &= 0, \end{aligned} \quad (3)$$

where the in-plane longitudinal and shear wavenumbers are defined as

$$k_l = \omega \sqrt{\frac{\rho(1-\nu^2)}{E}} \quad \text{and} \quad k_t = \omega \sqrt{\frac{2\rho(1+\nu)}{E}}. \quad (4)$$

At each point of the boundary Γ ($= \partial\Omega_s$) two boundary conditions must be specified. Three groups of boundary conditions are considered ($\Gamma = \Gamma_v \cup \Gamma_t \cup \Gamma_{vt}$):

- *Kinematic boundary conditions*: the displacement components are specified along the boundary. These conditions are expressed as

$$\left. \begin{aligned} R_{w_n}(\mathbf{x}) = \mathcal{L}_{w_n} \begin{bmatrix} e(\mathbf{x}) \\ \Omega(\mathbf{x}) \end{bmatrix} - \bar{w}_n(\mathbf{x}) = 0 \\ R_{w_s}(\mathbf{x}) = \mathcal{L}_{w_s} \begin{bmatrix} e(\mathbf{x}) \\ \Omega(\mathbf{x}) \end{bmatrix} - \bar{w}_s(\mathbf{x}) = 0 \end{aligned} \right\} \quad \mathbf{x} \in \Gamma_v, \quad (5)$$

with \bar{w}_n and \bar{w}_s the prescribed values for the displacement components. A fixed edge is a special case with zero values prescribed.

- *Mechanical boundary conditions*: the stress resultants have prescribed values:

$$\left. \begin{aligned} R_{T_n}(\mathbf{x}) = \mathcal{L}_{T_n} \begin{bmatrix} e(\mathbf{x}) \\ \Omega(\mathbf{x}) \end{bmatrix} - \bar{T}_n(\mathbf{x}) = 0 \\ R_{T_s}(\mathbf{x}) = \mathcal{L}_{T_s} \begin{bmatrix} e(\mathbf{x}) \\ \Omega(\mathbf{x}) \end{bmatrix} - \bar{T}_s(\mathbf{x}) = 0 \end{aligned} \right\} \quad \mathbf{x} \in \Gamma_t, \quad (6)$$

with \bar{T}_n and \bar{T}_s the prescribed values for the in-plane normal and tangential forces. A free edge is a special case with zero values prescribed for the force resultants.

- *Mixed boundary conditions*: both a displacement and a traction component are prescribed. Following the terminology of Bardell [3], these conditions are called simply supported analogous to plate bending problems. There exist two feasible boundary conditions in this group $\Gamma_{vt} = \Gamma_{vt1} \cup \Gamma_{vt2}$ [14],

$$\left. \begin{aligned} R_{w_s}(\mathbf{x}) = \mathcal{L}_{w_s} \begin{bmatrix} e(\mathbf{x}) \\ \Omega(\mathbf{x}) \end{bmatrix} - \bar{w}_s(\mathbf{x}) = 0 \\ R_{T_n}(\mathbf{x}) = \mathcal{L}_{T_n} \begin{bmatrix} e(\mathbf{x}) \\ \Omega(\mathbf{x}) \end{bmatrix} - \bar{T}_n(\mathbf{x}) = 0 \end{aligned} \right\} \mathbf{x} \in \Gamma_{vt1}, \quad (7)$$

and

$$\left. \begin{aligned} R_{w_n}(\mathbf{x}) = \mathcal{L}_{w_n} \begin{bmatrix} e(\mathbf{x}) \\ \Omega(\mathbf{x}) \end{bmatrix} - \bar{w}_n(\mathbf{x}) = 0 \\ R_{T_s}(\mathbf{x}) = \mathcal{L}_{T_s} \begin{bmatrix} e(\mathbf{x}) \\ \Omega(\mathbf{x}) \end{bmatrix} - \bar{T}_s(\mathbf{x}) = 0 \end{aligned} \right\} \mathbf{x} \in \Gamma_{vt2}. \quad (8)$$

For a simply supported edge the prescribed values, \bar{w}_s and \bar{T}_n for the first set or \bar{w}_n and \bar{T}_s for the second set, are zero.

The differential operators for the in-plane normal and tangential displacement and the in-plane normal and tangential force are defined as follows:

$$\begin{aligned} \mathcal{L}_{w_n} &= \left[-\frac{1}{k_t^2} \frac{\partial}{\partial n} \quad \frac{1}{k_t^2} \frac{\partial}{\partial s} \right], \\ \mathcal{L}_{w_s} &= \left[-\frac{1}{k_t^2} \frac{\partial}{\partial s} \quad -\frac{1}{k_t^2} \frac{\partial}{\partial n} \right], \\ \mathcal{L}_{T_n} &= \left[-\frac{1}{k_t^2} \frac{Eh}{(1-\nu^2)} \left(\frac{\partial^2}{\partial n^2} + \nu \frac{\partial^2}{\partial s^2} \right) \quad \frac{1}{k_t^2} \frac{Eh}{(1+\nu)} \frac{\partial^2}{\partial n \partial s} \right], \\ \mathcal{L}_{T_s} &= \left[-\frac{1}{k_t^2} \frac{Eh}{(1+\nu)} \frac{\partial^2}{\partial n \partial s} \quad \frac{1}{k_t^2} \frac{Eh}{2(1+\nu)} \left(\frac{\partial^2}{\partial s^2} - \frac{\partial^2}{\partial n^2} \right) \right]. \end{aligned} \quad (9)$$

where n and s are, respectively, the in-plane normal and in-plane tangential directions of the boundary (see Fig. 1).

3. STRESS SINGULARITIES

In a polygonal domain, singular strains and stresses can appear in the corner points. The singularity arises when the internal angle α formed by the two edges of the corner exceeds a critical value. The critical value depends on the boundary conditions applied along the two adjacent edges of the corner point. This section discusses the singular behaviour in the vicinity of such a corner. For that purpose, an analytical solution is defined, which approximates asymptotically the displacement field and stresses in the vicinity of the corner. The aim of the asymptotic analysis is twofold:

- it allows to predict the behaviour of possible corner singularities based on the problem geometry and applied boundary conditions,
- it allows to define functions that accurately represent the singular behaviour in the corner and that can be included as special purpose functions in the set of basis functions of the envisaged wave models (see Sec. 4).

To define the analytical solution in the vicinity of a corner point, some assumptions are made. To start with, it is assumed that the stresses within a small vicinity of the corner are hardly affected by the boundary conditions away from the corner point. The far-field loading in the global configuration will only determine whether a local singular stress field participates in a particular global configuration or not. Therefore, it is appropriate to study the behaviour in the vicinity of a corner by means of an infinite wedge domain, as shown in Fig. 2. The solutions of the infinite wedge domain are nevertheless applied for finite structures. However, they approximate the singular behaviour very well in the vicinity of the corner, provided that the internal angle and radial boundary conditions of the infinite wedge correspond to those of the corner in the actual problem. Furthermore, only wedges comprised of a single linear elastic material are considered. In conclusion, to analyse the stress fields in the vicinity of a certain corner, an infinite wedge domain with identical internal angle and radial boundary conditions is defined.

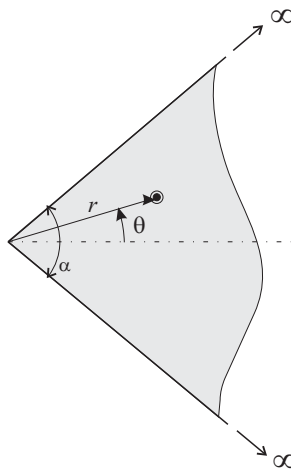


Fig. 2. An infinite wedge domain.

For the wedge domain the homogeneous, analytical solution for the in-plane displacements w_x and w_y is formulated. This analytical solution needs to satisfy:

- (i) the homogeneous, dynamic equation,
- (ii) two regularity conditions in the corner point,
- (iii) the radial boundary conditions.

Starting from the exact analytical displacement field, the strains or stresses and their singular behaviour can be evaluated.

In addition, the defined dynamic solution is compared with the static solutions for the infinite wedge domain, which were originally defined by Williams [39]. In this case, the solution must satisfy the homogeneous static differential equation rather than the dynamic equation. The problem geometry and boundary conditions remain identical as in the dynamic problem. The discussion of the static solutions consists of three main parts:

- First, the static solutions defined by Williams are discussed. It is demonstrated that for simply supported edges the singularities in the static and dynamic solutions exhibit an identical asymptotic behaviour in the vicinity of the corner point. For other combinations of radial boundary conditions, it is impossible to define an exact dynamic solution that satisfies the boundary conditions. However, it is assumed that the asymptotic behaviour of the singularities in the static and dynamic solutions is also identical for other combinations of boundary conditions than simply supported. Consequently, an approximate dynamic solution can be derived from the static eigenfunctions such that its singular behaviour is asymptotically accurate. This approximate

dynamic solution will still satisfy the governing dynamic equations. Only the radial boundary conditions are not exactly fulfilled.

- In addition to the singularities defined by Williams, the possibility exists that logarithmic contributions to the stress singularities appear [29]. Logarithmic stress singularities only occur for a few specific values of the internal angle α , which depend on the considered problem and applied boundary conditions. At this moment, it is impossible to derive a dynamic solution that accurately represents the logarithmic singularities in the stress field.
- Finally, static problems with inhomogeneous boundary conditions are considered. In this case, the solution consists of the fields that satisfy the corresponding homogeneous problem and the fields that satisfy the inhomogeneous problem. It is assumed that also for inhomogeneous problems the singularities in the static and dynamic solution have the same asymptotic behaviour. This allows to derive an approximate dynamic solution, provided that no logarithmic stresses are present.

The obtained dynamic solutions accurately represent the singular behaviour in the vicinity of the corner and they can consequently be included as special purpose functions in the set of basis functions of the WBM. Since the set of dynamic solutions does not form a complete function set, they can only be used in combination with the conventional set of wave functions (see Sec. 4).

3.1. Analytical solution infinite wedge domain

The homogeneous solution for the in-plane displacement field is defined starting from the uncoupled differential equations (3) for the dilatational and rotational strain. Assuming a separable function for the strains $e(r, \theta)$ and $\Omega(r, \theta)$ in the polar coordinates indicated in Fig. 2 ($-\alpha/2 \leq \theta \leq \alpha/2$), leads to the following homogeneous solution:

$$e = \sum_{k=1}^{\infty} \left[\cos(\lambda_{lk}\theta) R_{\lambda_{lk}}(k_l r) + \sin(\lambda_{lk}^*\theta) R_{\lambda_{lk}^*}(k_l r) \right],$$

$$\Omega = \sum_{k=1}^{\infty} \left[\cos(\lambda_{tk}\theta) R_{\lambda_{tk}}(k_t r) + \sin(\lambda_{tk}^*\theta) R_{\lambda_{tk}^*}(k_t r) \right],$$
(10)

where

$$R_{\lambda}(z) = A_{\lambda} J_{\lambda}(z) + B_{\lambda} Y_{\lambda}(z).$$
(11)

The eigenvalues are defined as $\lambda_l = \lambda_{lk}$ or λ_{lk}^* for the dilatational strain and $\lambda_t = \lambda_{tk}$ or λ_{tk}^* for the rotational strain. A_{λ} and B_{λ} are two constants of integration and, J_{λ} and Y_{λ} are the ordinary and modified Bessel functions of the first kind. The eigenfunctions associated with λ_{lk} and λ_{tk} describe the symmetric strain fields with respect to the axes $\theta = 0$; the ones associated with λ_{lk}^* and λ_{tk}^* are anti-symmetric with respect to this axes. Application of the radial boundary conditions at $\theta = \pm\alpha/2$ to the homogeneous solution (10) yields a set of equations in the unknown integration constants:

$$\mathbf{A}\mathbf{c} = \mathbf{0},$$
(12)

with \mathbf{A} the coefficient matrix and \mathbf{c} the vector of integration constants. To eliminate the trivial solutions, the determinant of the coefficient matrix must vanish:

$$\det \mathbf{A} = 0.$$
(13)

The eigenvalues λ_{lk} , λ_{tk} , λ_{lk}^* and λ_{tk}^* are the solutions of this characteristic equation.

Imposing independent conditions for $r = \infty$ and $r = 0$ leads to the integration constants of each eigenfunction. Since the conditions at infinity have no influence on the singular behaviour in the corner, they can be discarded. The absence of conditions at infinity merely results in solutions that are non-unique. Since the only objective of these functions is the characterisation of all possible displacement and stress distributions at the corner point, their non-uniqueness does not create any problem. At the wedge tip $r = 0$, the following regularity conditions are imposed:

$$\begin{aligned} w_r(0, \theta) &= \text{finite}, \\ w_\theta(0, \theta) &= \text{finite}. \end{aligned} \tag{14}$$

Imposing these conditions ensures the boundedness of the strain energies as proved by Knowles [17]. Transformation of the in-plane displacements to the strain components according to Eq. (2) and introduction of the eigenfunctions R_λ (11) lead to the following conditions:

$$\begin{aligned} w_r(r, \theta)|_{r=0} &= \lim_{r \rightarrow 0} \left[-\frac{1}{k_l^2} \frac{\partial e}{\partial r} + \frac{1}{k_t^2} \frac{1}{r} \frac{\partial \Omega}{\partial \theta} \right] \\ &= \lim_{r \rightarrow 0} \left[c_1(\theta) [A_{\lambda_l} (J_{\lambda_l-1}(k_l r) - J_{\lambda_l+1}(k_l r)) + B_{\lambda_l} (Y_{\lambda_l-1}(k_l r) - Y_{\lambda_l+1}(k_l r))] \right. \\ &\quad \left. + c_2(\theta) \frac{1}{r} [A_{\lambda_t} J_{\lambda_t}(k_t r) + B_{\lambda_t} Y_{\lambda_t}(k_t r)] \right] = \text{finite}, \end{aligned} \tag{15}$$

$$\begin{aligned} w_\theta(r, \theta)|_{r=0} &= \lim_{r \rightarrow 0} \left[-\frac{1}{k_l^2} \frac{1}{r} \frac{\partial e}{\partial \theta} - \frac{1}{k_t^2} \frac{\partial \Omega}{\partial r} \right] \\ &= \lim_{r \rightarrow 0} \left[c_3(\theta) \frac{1}{r} [A_{\lambda_l} J_{\lambda_l}(k_l r) + B_{\lambda_l} Y_{\lambda_l}(k_l r)] + c_4(\theta) [A_{\lambda_t} (J_{\lambda_t-1}(k_t r) - J_{\lambda_t+1}(k_t r)) \right. \\ &\quad \left. + B_{\lambda_t} (Y_{\lambda_t-1}(k_t r) - Y_{\lambda_t+1}(k_t r))] \right] = \text{finite}, \end{aligned}$$

where the functions $c_\bullet(\theta)$ only depend on the angular coordinate θ . Since

$$\lim_{z \rightarrow 0} Y_\lambda(z) = -\infty \tag{16}$$

the regularity conditions can only be satisfied if $B_\lambda = 0$. The remaining expressions are finite if

$$\lambda_l > 1 \quad \text{and} \quad \lambda_t > 1. \tag{17}$$

Thus, the regularity conditions at the corner point yield the following eigenfunctions:

$$\begin{aligned} R_{\lambda_l} &= A_{\lambda_l} J_{\lambda_l}(k_l r), \quad \lambda_l > 1, \\ R_{\lambda_t} &= A_{\lambda_t} J_{\lambda_t}(k_t r), \quad \lambda_t > 1, \end{aligned} \tag{18}$$

where $\lambda_l = \lambda_{lk}$ or λ_{lk}^* and $\lambda_t = \lambda_{tk}$ or λ_{tk}^* depending on whether the eigenvalues are associated with a symmetric or anti-symmetric eigenfunction. These eigenfunctions correspond with the admissible displacement fields:

$$\begin{aligned}
w_r &= -\frac{1}{2k_l} \left[A_{\lambda_{lk}} \cos(\lambda_{lk}\theta) (J_{\lambda_{lk}-1}(k_l r) - J_{\lambda_{lk}+1}(k_l r)) \right. \\
&\quad \left. + A_{\lambda_{lk}^*} \sin(\lambda_{lk}^*\theta) (J_{\lambda_{lk}^*-1}(k_l r) - J_{\lambda_{lk}^*+1}(k_l r)) \right] \\
&\quad + \frac{1}{k_t^2 r} \left[-A_{\lambda_t} \lambda_t \sin(\lambda_t \theta) J_{\lambda_t}(k_t r) + A_{\lambda_t^*} \lambda_t^* \cos(\lambda_t^* \theta) J_{\lambda_t^*}(k_t r) \right], \\
w_\theta &= \frac{1}{k_l^2 r} \left[A_{\lambda_{lk}} \lambda_{lk} \sin(\lambda_{lk}\theta) J_{\lambda_{lk}}(k_l r) - A_{\lambda_{lk}^*} \lambda_{lk}^* \cos(\lambda_{lk}^*\theta) J_{\lambda_{lk}^*}(k_l r) \right] \\
&\quad - \frac{1}{2k_t} \left[A_{\lambda_{tk}} \cos(\lambda_{tk}\theta) (J_{\lambda_{tk}-1}(k_t r) - J_{\lambda_{tk}+1}(k_t r)) \right. \\
&\quad \left. + A_{\lambda_{tk}^*} \sin(\lambda_{tk}^*\theta) (J_{\lambda_{tk}^*-1}(k_t r) - J_{\lambda_{tk}^*+1}(k_t r)) \right],
\end{aligned} \tag{19}$$

with $\lambda_l > 1$ and $\lambda_t > 1$.

3.2. Singularities in the stress field

Starting from the analytical solution, the strain and stress fields can be evaluated in the vicinity of the corner. The strains are expressed as

$$\begin{aligned}
\epsilon_r &= \frac{\partial w_r}{\partial r}, \\
\epsilon_\theta &= \frac{1}{r} \frac{\partial w_\theta}{\partial \theta} + \frac{w_r}{r}, \\
\epsilon_{r\theta} &= \frac{1}{r} \frac{\partial w_r}{\partial \theta} + \frac{\partial w_\theta}{\partial r} - \frac{w_\theta}{r}.
\end{aligned} \tag{20}$$

The stresses in a homogeneous and isotropic medium are defined as

$$\begin{aligned}
\sigma_r &= \frac{E}{1-\nu^2} \left(\frac{\partial w_r}{\partial r} + \frac{\nu}{r} \frac{\partial w_\theta}{\partial \theta} + \nu \frac{w_r}{r} \right), \\
\sigma_\theta &= \frac{E}{1-\nu^2} \left(\nu \frac{\partial w_r}{\partial r} + \frac{1}{r} \frac{\partial w_\theta}{\partial \theta} + \frac{w_r}{r} \right), \\
\tau_{r\theta} &= \frac{E}{2(1+\nu)} \left(\frac{1}{r} \frac{\partial w_r}{\partial \theta} + \frac{\partial w_\theta}{\partial r} - \frac{w_\theta}{r} \right).
\end{aligned} \tag{21}$$

Substitution of the eigenfunctions (18) associated with eigenvalues λ_l and λ_t in the expression of the radial stress σ_r results in

$$\begin{aligned}
\sigma_r &= \frac{E}{1-\nu^2} \left[-\frac{A_{\lambda_l}}{k_l^2} \left(\frac{k_l^2}{4} J_{\lambda_l-2}(k_l r) + \frac{\nu k_l}{2r} J_{\lambda_l-1}(k_l r) - \left(\frac{k_l^2}{2} + \frac{\nu}{r^2} \right) J_{\lambda_l}(k_l r) \right. \right. \\
&\quad \left. \left. - \frac{\nu k_l}{2r} J_{\lambda_l+1} + \frac{k_l^2}{4} J_{\lambda_l+2} \right) + (1-\nu) \frac{A_{\lambda_t}}{k_t^2 r} \left(\frac{k_t}{2} J_{\lambda_t-1}(k_t r) - \frac{1}{r} J_{\lambda_t}(k_t r) - \frac{k_t}{2} J_{\lambda_t+1}(k_t r) \right) \right].
\end{aligned} \tag{22}$$

Use of the power series expansion for the Bessel function of the first kind [1],

$$J_\lambda(z) = \sum_{n=0}^{\infty} \frac{(-1)^n \left(\frac{z}{2}\right)^{2n+\lambda}}{n! \Gamma(n+\lambda+1)}, \tag{23}$$

leads to the following expression for the radial stress in the vicinity of the corner point:

$$\sigma_r|_{r=0} = \lim_{r \rightarrow 0} \left[\left(\frac{1}{\Gamma(\lambda_l - 1)} + \nu \frac{1}{\Gamma(\lambda_l)} - \nu \frac{1}{\Gamma(\lambda_l + 1)} \right) r^{\lambda_l - 2} + \left(\frac{1}{\Gamma(\lambda_t)} - \frac{1}{\Gamma(\lambda_t + 1)} \right) r^{\lambda_t - 2} \right]. \quad (24)$$

Equation (24) shows that the stress field becomes singular in the corner point if one of the eigenvalues becomes smaller than 2, $\lambda_l < 2$ or $\lambda_t < 2$. The order of the singularity is $\lambda - 2$. The two other stress components σ_θ and $\tau_{r\theta}$ can be approximated in the same manner. The order of these singularities is $\lambda - 2$ as well.

3.3. Simply supported infinite wedge domain

In this section, the analytical solution is defined for an infinite wedge domain where both edges are simply supported. The conditions are formulated following the second group of conditions Γ_{vt2} , which in polar coordinates are expressed as

$$\begin{aligned} w_\theta \left(r, \pm \frac{\alpha}{2} \right) &= 0, \\ \tau_{r\theta} \left(r, \pm \frac{\alpha}{2} \right) &= 0. \end{aligned} \quad (25)$$

Application of these boundary conditions to the homogeneous solution (19) and solution of the resulting characteristic equation yields the eigenvalues:

$$\begin{aligned} \lambda_{lk} &= \frac{2k\pi}{\alpha}, & \lambda_{tk} &= (2k - 1) \frac{\pi}{\alpha}, \\ \lambda_{lk}^* &= (2k - 1) \frac{\pi}{\alpha}, & \lambda_{tk}^* &= \frac{2k\pi}{\alpha} \end{aligned} \quad (26)$$

with $k = 1, 2, \dots$. The homogeneous solutions (19) together with the here defined eigenvalues form an exact analytical solution for the simply supported infinite wedge since they satisfy the dynamic equations, the regularity conditions and the radial boundary conditions. As stated in the previous section, singular stresses can be expected when one of the eigenvalues becomes smaller than 2. For a simply supported corner, the critical angle α , starting from which singularities can occur, equals thus $\pi/2$ or 90° .

This is illustrated with an example. Consider a simply supported wedge with internal angle $\alpha = 100^\circ$. The in-plane longitudinal and shear wavenumbers k_l and k_t equal 12.0 m^{-1} and 20.2 m^{-1} , respectively. In this case, the smallest eigenvalues are:

$$\begin{aligned} \lambda_l &= 3.6, 7.2, \dots, & \lambda_t &= 1.8, 5.4, \dots, \\ \lambda_l^* &= 1.8, 5.4, \dots, & \lambda_t^* &= 3.6, 7.2, \dots \end{aligned} \quad (27)$$

The first eigenvalue of the anti-symmetric dilatational and symmetric rotational strain field λ_l^* and λ_t are smaller than 2 such that the stress field corresponding to these eigenfunctions will exhibit a singularity. The remaining eigenvalues do not induce a singularity. Figure 3 shows the radial and angular displacement field corresponding to the eigenfunctions with $\lambda_l^* = \lambda_t = 1.8$. It is seen that the displacement boundary conditions are fulfilled along the two radial edges. Figure 4 shows the radial stress field which corresponds to these eigenfunctions. As expected the stress field becomes singular in the corner point.

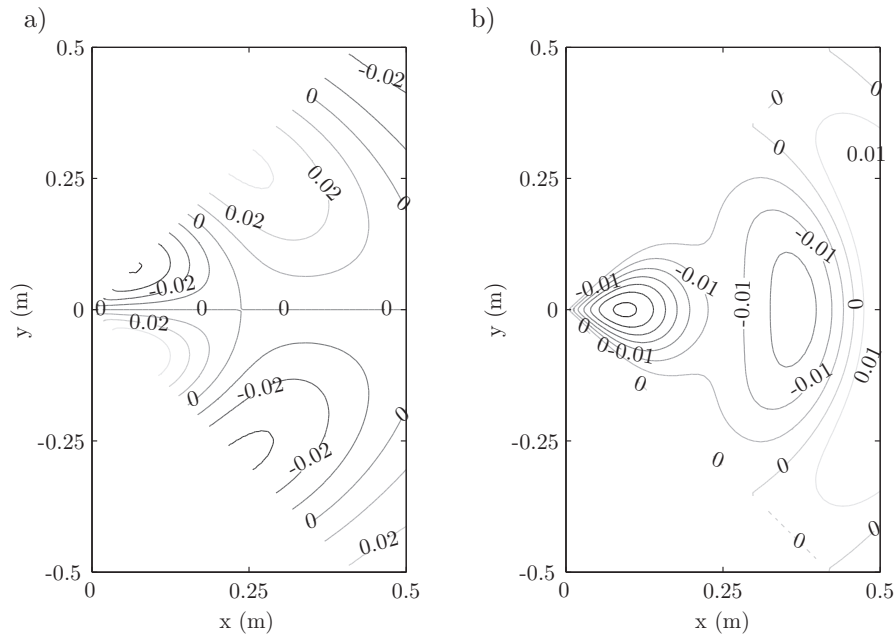


Fig. 3. Displacement field corresponding to the anti-symmetric dilatational and symmetric rotational eigenfunctions with $\lambda_l^* = \lambda_t = 1.8$ for a simply supported infinite wedge with $\alpha = 100^\circ$, $k_l = 12.0 \text{ m}^{-1}$ and $k_t = 20.2 \text{ m}^{-1}$: a) radial displacement w_r , b) angular displacement w_θ .

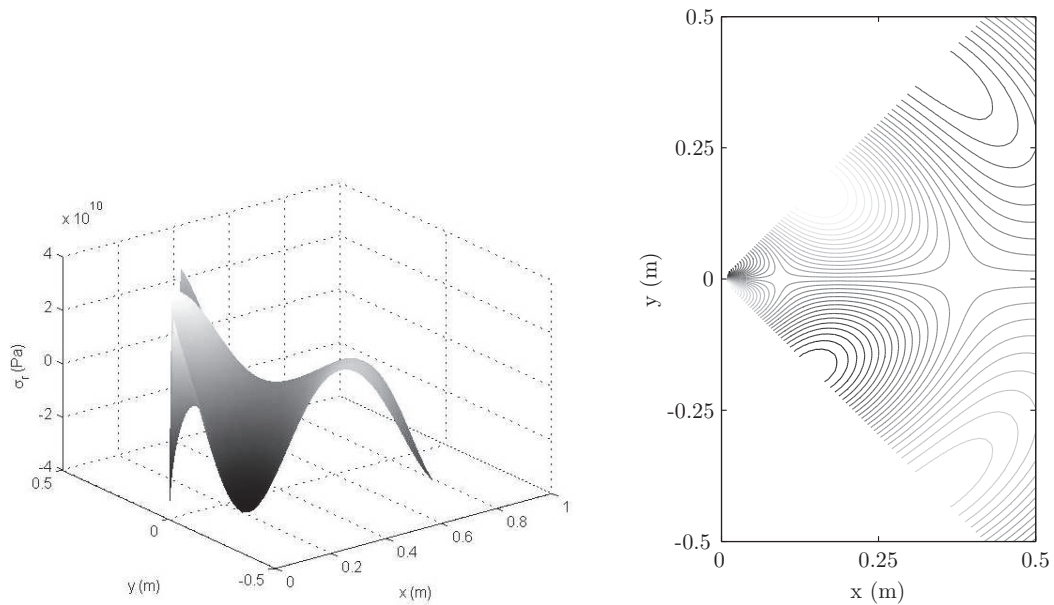


Fig. 4. Radial stress field corresponding to the anti-symmetric dilatational and symmetric rotational eigenfunctions with $\lambda_l^* = \lambda_t = 1.8$ for a simply supported infinite wedge with $\alpha = 100^\circ$, $k_l = 12.0 \text{ m}^{-1}$ and $k_t = 20.2 \text{ m}^{-1}$.

3.4. Analytical solutions of the static infinite wedge

In this section, the previously defined dynamic solution is compared with the static solution for the infinite wedge domain. In this case, the analytical solution needs to satisfy the homogeneous, static equations instead of the dynamic equations, namely Eq. (3) with $k_l = k_t = 0$. The radial boundary conditions and regularity conditions remain identical. Williams [39] was the first to define the analytical solutions for a static infinite wedge domain, introducing the following displacement fields:

$$\begin{aligned}
w_r &= -\frac{r^{\lambda_s}}{2G} [A_{\lambda_s} \cos(\lambda_s + 1)\theta + B_{\lambda_s} \sin(\lambda_s + 1)\theta \\
&\quad + (\lambda_s - k)(C_{\lambda_s} \cos(\lambda_s - 1)\theta + D_{\lambda_s} \sin(\lambda_s - 1)\theta)], \\
w_\theta &= \frac{r^{\lambda_s}}{2G} [A_{\lambda_s} \sin(\lambda_s + 1)\theta - B_{\lambda_s} \cos(\lambda_s + 1)\theta \\
&\quad + (\lambda_s + k)(C_{\lambda_s} \sin(\lambda_s - 1)\theta - D_{\lambda_s} \cos(\lambda_s - 1)\theta)],
\end{aligned} \tag{28}$$

with G the shear modulus and $k = (3 - \nu)/(1 + \nu)$ for plane stress problems. The corresponding stresses are defined as

$$\begin{aligned}
\sigma_r &= -\lambda_s r^{\lambda_s - 1} [A_{\lambda_s} \cos(\lambda_s + 1)\theta + B_{\lambda_s} \sin(\lambda_s + 1)\theta \\
&\quad + (\lambda_s - 3)(C_{\lambda_s} \cos(\lambda_s - 1)\theta + D_{\lambda_s} \sin(\lambda_s - 1)\theta)], \\
\sigma_\theta &= \lambda_s r^{\lambda_s - 1} [A_{\lambda_s} \cos(\lambda_s + 1)\theta + B_{\lambda_s} \sin(\lambda_s + 1)\theta \\
&\quad + (\lambda_s + 1)(C_{\lambda_s} \cos(\lambda_s - 1)\theta + D_{\lambda_s} \sin(\lambda_s - 1)\theta)], \\
\tau_{r\theta} &= \lambda_s r^{\lambda_s - 1} [A_{\lambda_s} \sin(\lambda_s + 1)\theta - B_{\lambda_s} \cos(\lambda_s + 1)\theta \\
&\quad + (\lambda_s - 1)(C_{\lambda_s} \sin(\lambda_s - 1)\theta - D_{\lambda_s} \cos(\lambda_s - 1)\theta)].
\end{aligned} \tag{29}$$

In the literature, no distinction is made between eigenvalues which correspond to a symmetric or anti-symmetric strain field. Therefore, that notation is also followed in this text. Eigenvalues λ_s with a negative real part are excluded, since they introduce a singular displacement field that is inconsistent with the regularity conditions. Furthermore, it is seen that eigenvalues $\lambda_s < 1$ give rise to singular stresses in the corner point. Comparing the radial stress fields for the static and dynamic solutions, i.e. Eq. (29) and Eq. (24), it is observed that the stresses have the same asymptotic behaviour in the vicinity of the corner point, provided that $\lambda_l = \lambda_s + 1$ and $\lambda_t = \lambda_s + 1$.

For the static wedge with simply supported edges, Seweryn [27] defines the eigenvalues as

$$\lambda_s = \frac{n\pi}{\alpha} - 1, \quad \lambda_s = \frac{n\pi}{\alpha} + 1, \tag{30}$$

where $n = 1, 2, \dots$. These eigenvalues are deduced from the application of the simply supported boundary conditions. Imposing the boundary conditions (25) to the homogeneous solution (28) yields a set of equations:

$$r^{\lambda_s - 1} \mathbf{A} \begin{Bmatrix} A_{\lambda_s} \\ B_{\lambda_s} \\ C_{\lambda_s} \\ D_{\lambda_s} \end{Bmatrix} = \mathbf{0}, \tag{31}$$

with \mathbf{A} the 4×4 coefficient matrix. To eliminate the trivial solutions, the determinant of \mathbf{A} must vanish, such that the resulting characteristic equation is satisfied:

$$\det \mathbf{A} = 0. \tag{32}$$

The static eigenvalues are compared with the dynamic values, derived in the previous section. Considering the first group of static eigenvalues (30), the range of n is subdivided into a set with even numbers and a set with odd numbers.

- *n even:*

By substitution of these eigenvalues in the system of equations (31) resulting from application of the radial boundary conditions, while taking into account that

$$\sin(\lambda_s + 1) \frac{\alpha}{2} = 0, \tag{33}$$

the integration constants can be determined:

$$B_{\lambda_s} = C_{\lambda_s} = D_{\lambda_s} = 0, \quad A_{\lambda_s} \neq 0. \quad (34)$$

The angular displacement field corresponding to these eigenvalues is anti-symmetric with respect to the axes $\theta = 0$:

$$w_\theta = r^{\lambda_s} \sin(\lambda_s + 1)\theta. \quad (35)$$

The radial displacement field is symmetric with respect to the θ -axes:

$$w_r = r^{\lambda_s} \cos(\lambda_s + 1)\theta. \quad (36)$$

For the dynamic displacement field, an anti-symmetric angular and symmetric radial displacement field is induced by the eigenvalues λ_{lk} and λ_{tk}^* , see Eq. (19). For the simply supported wedge, these dynamic eigenvalues are defined as

$$\lambda_{lk} = \lambda_{tk}^* = \frac{2k\pi}{\alpha}, \quad (37)$$

with $k = 1, 2, \dots$. Hence, the following relation:

$$\lambda = \lambda_s + 1, \quad (38)$$

between static and dynamic eigenvalues is valid. Considering the asymptotic behaviour of the stresses in the vicinity of the corner point, it is seen that the static and dynamic solution for the radial stress are asymptotically identical:

$$\begin{aligned} \sigma_r &\sim r^{\lambda_s - 1} && \text{for the static wedge,} \\ \sigma_r &\sim r^{\lambda_l - 2} + r^{\lambda_t^* - 2} && \text{for the dynamic wedge.} \end{aligned} \quad (39)$$

- *n odd:*

We proceed in a similar way. Substitution of the eigenvalues in the system of equations leads to the constants:

$$A_{\lambda_s} = C_{\lambda_s} = D_{\lambda_s} = 0, \quad B_{\lambda_s} \neq 0. \quad (40)$$

In this case, the corresponding angular displacement field is symmetric with respect to the axes $\theta = 0$, whereas the radial displacement field is anti-symmetric:

$$\begin{aligned} w_\theta &= r^{\lambda_s} \cos(\lambda_s + 1)\theta, \\ w_r &= r^{\lambda_s} \sin(\lambda_s + 1)\theta. \end{aligned} \quad (41)$$

For the dynamic displacement field, the eigenvalues λ_{lk}^* and λ_{tk} provoke a symmetric angular and anti-symmetric radial displacement field, see Eq. (19). For the simply supported wedge, these dynamic eigenvalues are defined as

$$\lambda_{lk}^* = \lambda_{tk} = (2k - 1) \frac{\pi}{\alpha}, \quad (42)$$

with $k = 1, 2, \dots$. Also for odd values of n , the relation

$$\lambda = \lambda_s + 1 \quad (43)$$

between static and dynamic eigenvalues is valid. Considering the asymptotic behaviour of the stresses in the vicinity of the corner point, it is seen that the static and dynamic solution for the stresses are identical,

$$\begin{aligned} \sigma_r &\sim r^{\lambda_s - 1} && \text{for the static wedge,} \\ \sigma_r &\sim r^{\lambda_l^* - 2} + r^{\lambda_t - 2} && \text{for the dynamic wedge.} \end{aligned} \quad (44)$$

For the second group of static eigenvalues $(30)_2$ no equivalent dynamic eigenvalues exist. However, these eigenvalues are always larger than 1 such that they do not induce any singularity in the stress field. Since the only objective of this study is the characterisation of stress singularities, the second group of static eigenvalues is not relevant and therefore not further considered. In summary, it is demonstrated that, for the simply supported infinite wedge, the singularities in the static and dynamic stress field are asymptotically identical in the vicinity of the corner point. It is assumed that the asymptotic behaviour of the singularities in the static and dynamic solution remains identical for all combinations of boundary conditions.

In a similar study of the infinite wedge domain, Bogy found conditions under which logarithmic stress singularities exist [7]. He states that these auxiliary fields can be generated by differentiating the original fields with respect to λ_s :

$$\begin{aligned}
 w_r = -\frac{r^{\lambda_s}}{2G} & \left[(A'_{\lambda_s} \cos(\lambda_s + 1)\theta + B'_{\lambda_s} \sin(\lambda_s + 1)\theta) \ln r \right. \\
 & + (1 + (\lambda_s - k) \ln r) (C'_{\lambda_s} \cos(\lambda_s - 1)\theta + D'_{\lambda_s} \sin(\lambda_s - 1)\theta) \\
 & \quad - \theta (A'_{\lambda_s} \sin(\lambda_s + 1)\theta - B'_{\lambda_s} \cos(\lambda_s + 1)\theta) \\
 & \quad \left. + (\lambda_s - k) (C'_{\lambda_s} \sin(\lambda_s - 1)\theta - D'_{\lambda_s} \cos(\lambda_s - 1)\theta) \right], \quad (45) \\
 w_\theta = \frac{r^{\lambda_s}}{2G} & \left[(A'_{\lambda_s} \sin(\lambda_s + 1)\theta - B'_{\lambda_s} \cos(\lambda_s + 1)\theta) \ln r \right. \\
 & + (1 + (\lambda_s + k) \ln r) (C'_{\lambda_s} \sin(\lambda_s - 1)\theta - D'_{\lambda_s} \cos(\lambda_s - 1)\theta) \\
 & \quad + \theta (A'_{\lambda_s} \cos(\lambda_s + 1)\theta + B'_{\lambda_s} \sin(\lambda_s + 1)\theta) \\
 & \quad \left. + (\lambda_s + k) (C'_{\lambda_s} \cos(\lambda_s - 1)\theta + D'_{\lambda_s} \sin(\lambda_s - 1)\theta) \right].
 \end{aligned}$$

The displacement fields (45) still satisfy the governing equations, since these equations are independent of λ_s . The auxiliary fields are supplemented to the original displacement fields (19) and the integration constants follow from application of the radial boundary conditions. As demonstrated in [28], the auxiliary fields can appear when

$$\mathcal{D} = 0 \quad \text{and} \quad \frac{\partial^n \mathcal{D}}{\partial \lambda_s^n} = 0 \quad (46)$$

for $n = 1, \dots, n_A - r_A$. \mathcal{D} is the determinant of the coefficient matrix \mathbf{A} resulting from application of the radial boundary conditions, n_A is the order of this matrix and r_A is its rank for the eigenvalue λ_s . In the neighbourhood of the corner, the stresses behave asymptotically as

$$\sigma \sim r^{\lambda_s - 1} \ln r + r^{\lambda_s - 1}. \quad (47)$$

Compared with the original fields, the stress fields contain an additional logarithmic term $\ln r$. The stresses now become singular when $\lambda_s \leq 1$. Logarithmic intensification of stress singularities can be viewed as a transition state between pure power singularities (λ_s real) and oscillatory power singularities (λ_s complex) [29]. A necessary but not sufficient condition is the occurrence of repeated roots of the eigenvalue equation. Dempsey [11] lists several configurations in which logarithmic intensification or pure logarithmic singularities ($\lambda_s = 1$) are present. Logarithmic singularities never appear for a range of internal angles. On the contrary, they only occur for a few specific angles α whose values normally depend on the applied boundary conditions and the material constants. For example, for the fixed-free infinite wedge logarithmic intensification occurs for corners with an internal angle [30],

$$\alpha = \pi - \alpha_k \quad \text{or} \quad \alpha = 2\pi - \alpha_k, \quad (48)$$

where α_k is defined as

$$\alpha_k = \sin^{-1} \frac{1}{\sqrt{1+\nu}}, \quad (49)$$

for $0 < \alpha_k \leq \pi/2$. In the dynamic solution for the infinite wedge, as defined in (19), no logarithmic intensification is present. Defining auxiliary dynamic fields by deriving the original fields with respect to the eigenvalue according to the procedure of Bogy [7], is impossible since no closed analytical expression exists for the derivative of a Bessel function with respect to its order. It is therefore impossible to make the static and dynamic solutions asymptotically equivalent only by adequately choosing the dynamic eigenvalues. As a result, currently no dynamic solution can be defined that accurately represents the singularities in the stress field when logarithmic intensification is present. Nevertheless, logarithmic stresses only occur in some specific configurations which form a minority.

In the case that the radial boundary conditions applied to the static infinite wedge are inhomogeneous, the solution consists of the fields that satisfy the corresponding homogeneous problem supplemented with the fields of the inhomogeneous problem. The inhomogeneous fields are obtained in a similar way as for the homogeneous conditions. The displacement fields are defined as in Eq. (28). If necessary, the original displacement fields are extended with the auxiliary displacement fields (45). Application of the radial boundary conditions, which in this case are inhomogeneous, leads to a system of equations in the integration constants. Solution of this system results in the required displacement and stress fields. Inhomogeneous boundary conditions can possibly induce logarithmic singularities [28, 29]. Also in this case, logarithmic singularities only appear for specific angles α . For example, consider a wedge with internal angle α that is subjected to a uniform shear force along one edge while the other edge is free of stresses. In this problem logarithmic singularities can occur if $\alpha = \tan \alpha$ or $\alpha = 257.45^\circ$. Other examples of logarithmic stresses with inhomogeneous boundary conditions are given in reference [29]. Furthermore, the assumption is made that also for inhomogeneous boundary conditions the singularities in the static and dynamic solution have the same asymptotic behaviour. If stress singularities are absent from the static solution, no stress singularities are expected in the dynamic stress field. If singularities appear, an approximate dynamic solution will be derived from the static solution such that the asymptotic behaviour around the corner of both solutions is identical. As said before, logarithmic stress fields can not be represented correctly by the dynamic solution. However, the configurations in which logarithmic stresses are induced due to inhomogeneous boundary conditions, form a minority.

3.5. General infinite wedge domain

In case where the two radial edges of the infinite wedge domain are not both simply supported, it is impossible to define an exact dynamic solution that satisfies the radial boundary conditions in addition to the dynamic equations. For static problems, on the other hand, the analytical solutions exist for each possible combination of radial boundary conditions [29, 39]. Table 1 lists the

Table 1. Characteristic equations and critical angles α_c for the static infinite wedge domain.

BC	characteristic equation	α_c
fixed – fixed	$\sin \alpha \lambda_s = \pm \frac{1+\nu}{3-\nu} \lambda_s \sin \alpha$	180°
free – free	$\sin \alpha \lambda_s = \mp \lambda_s \sin \alpha$	180°
fixed – free	$\sin^2 \alpha \lambda_s = \frac{4}{(3-\nu)(1+\nu)} - \frac{1+\nu}{3-\nu} \lambda_s^2 \sin^2 \alpha$	60° ^a

^a the presented critical angle corresponds with a Poisson coefficient $\nu = 0.3$

characteristic equations for various combinations of homogeneous boundary conditions as defined by Williams.

In addition, Table 1 mentions the critical angles starting from which singularities may be expected. The critical angles are determined from the characteristic equations as the angles for which the smallest eigenvalue becomes smaller than 1. For corners with an internal angle larger than the critical angle, the expansion set of the WBM will need to be extended with the corner functions. However, the Williams functions cannot be incorporated in the WBM as basis functions. As will be shown in Sec. 4, the WBM is an indirect Trefftz method and thus it requires basis functions that exactly satisfy the dynamic equations. Only functions consistent with Eq. (19) satisfy the homogeneous, dynamic equations and can be used as basis functions. The corresponding characteristic eigenvalues λ are usually deduced from the radial boundary conditions. Since that is impossible in this case, they are chosen such that the singular behaviour around the corner is asymptotically the same as that of the corresponding static solution. The derivation of the dynamic eigenvalues from the static ones can only be performed for the original, basic stress fields. Subsection 3.4 presented the relation between static and dynamic eigenvalues that yields the same singular behaviour around the corner point. For an anti-symmetric angular or symmetric radial displacement field, the dynamic eigenvalues are defined as

$$\lambda_l = \lambda_s + 1 \quad \text{and} \quad \lambda_l^* = \lambda_s + 1. \quad (50)$$

For a symmetric angular or anti-symmetric radial displacement field, the dynamic eigenvalues are defined as

$$\lambda_l^* = \lambda_s + 1 \quad \text{and} \quad \lambda_l = \lambda_s + 1. \quad (51)$$

The resulting eigenfunctions satisfy the dynamic equations inherently such that they can be incorporated in the WBM as basis functions. Although the radial boundary conditions are not represented correctly by this derived solution, the singularity has the correct order and the stresses in the neighbourhood of the corner form a good approximation for those in the problem solution, at least when only power singularities are present. If logarithmic stresses are present, it is not yet possible to define a dynamic solution that approximates the stress singularity accurately.

4. BASIC CONCEPTS OF THE WAVE BASED METHOD

The FEM and WBM are both deterministic techniques, however they are based on different principles. Whereas the classical FEM uses (simple) polynomial shape functions, the WBM is based on the Trefftz principle and as a result uses exact solutions of the governing differential equations as basis functions. The WBM divides the domain into a small number of large subdomains. Provided that each of the subdomains is convex, the convergence of the method is ensured [12]. Since the basis functions satisfy the governing equations, minimisation of the approximation error induced in the boundary conditions and the conformity between subdomains leads to the solution of the system.

The specific choice of basis functions leads to a substantially reduced size of the numerical models, which leads to substantially lower computation times as compared to the FEM. As a result the WBM can be used up to considerably higher frequencies. This has been shown for interior and exterior (vibro-) acoustic problems [5, 22–24, 33, 37, 38], for the structural dynamic analysis of the bending of flat plates [34, 35] and for poro-elastic problems [9].

4.1. Division in convex subdomains

In the case of a non-convex problem geometry, the domain Ω_s must be divided in N_s non-overlapping convex subdomains $\Omega_s^{(\beta)}$ to guarantee convergence of the method. The coupling between the different subdomains is created by imposing a displacement compatibility and force equilibrium. The

displacement compatibility along the coupling interface $\Gamma_I^{(\beta,\alpha)}$ between subdomains β and α is formulated as

$$\left. \begin{aligned} R_{Iw_n}^{(\beta,\alpha)} &= w_n^{(\beta)}(\mathbf{x}) + w_n^{(\alpha)}(\mathbf{x}) = 0 \\ R_{Iw_s}^{(\beta,\alpha)} &= w_s^{(\beta)}(\mathbf{x}) + w_s^{(\alpha)}(\mathbf{x}) = 0 \end{aligned} \right\} \quad \mathbf{x} \in \Gamma_{I_v}^{(\beta,\alpha)}. \quad (52)$$

The force equilibrium between subdomains β and α corresponds with

$$\left. \begin{aligned} R_{IT_n}^{(\beta,\alpha)} &= T_n^{(\beta)}(\mathbf{x}) - T_n^{(\alpha)}(\mathbf{x}) = 0 \\ R_{IT_s}^{(\beta,\alpha)} &= T_s^{(\beta)}(\mathbf{x}) - T_s^{(\alpha)}(\mathbf{x}) = 0 \end{aligned} \right\} \quad \mathbf{x} \in \Gamma_{I_t}^{(\beta,\alpha)}. \quad (53)$$

The coupling conditions are formulated in terms of the boundary displacements and forces:

$$\begin{aligned} w_n^{(\beta)} &= \mathbf{n}^{(\beta)T} \begin{Bmatrix} w_x^{(\beta)} \\ w_y^{(\beta)} \end{Bmatrix}, & T_n^{(\beta)} &= \mathbf{n}^{(\beta)T} \begin{Bmatrix} T_x^{(\beta)} \\ T_y^{(\beta)} \end{Bmatrix}, \\ w_s^{(\beta)} &= \mathbf{s}^{(\beta)T} \begin{Bmatrix} w_x^{(\beta)} \\ w_y^{(\beta)} \end{Bmatrix}, & T_s^{(\beta)} &= \mathbf{s}^{(\beta)T} \begin{Bmatrix} T_x^{(\beta)} \\ T_y^{(\beta)} \end{Bmatrix}, \end{aligned} \quad (54)$$

where the vector $\mathbf{n}^{(\beta)}$ corresponds with the subdomain outward-normal direction, and the vector $\mathbf{s}^{(\beta)}$ with the tangential direction along the interface (see Fig. 5).

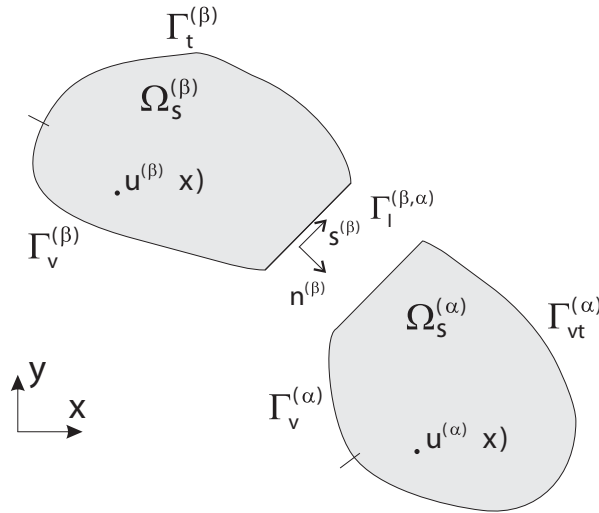


Fig. 5. Subdomain partitioning.

In the WBM, the continuity conditions are enforced using a direct coupling approach, i.e. the interface conditions are imposed directly as boundary conditions to the subdomains. In case that the displacement compatibility (52) between subdomains β and α is imposed as a boundary condition for domain β , $\Gamma_{I_v}^{(\beta,\alpha)}$ and $\Gamma_{I_t}^{(\beta,\alpha)}$ are defined as

$$\Gamma_{I_v}^{(\beta,\alpha)} = \Gamma_I^{(\beta,\alpha)} \quad \text{and} \quad \Gamma_{I_t}^{(\beta,\alpha)} = \emptyset. \quad (55)$$

When, on the contrary, the force equilibrium (53) is imposed on domain β , the following definitions hold:

$$\Gamma_{I_v}^{(\beta,\alpha)} = \emptyset \quad \text{and} \quad \Gamma_{I_t}^{(\beta,\alpha)} = \Gamma_I^{(\beta,\alpha)}. \quad (56)$$

The remaining continuity condition is imposed as boundary condition on domain α .

4.2. Field variable expansion

In each subdomain $\Omega_s^{(\beta)}$ the field variables are approximated by the solution expansion

$$\begin{Bmatrix} \widehat{w}_x^{(\beta)} \\ \widehat{w}_y^{(\beta)} \end{Bmatrix} = \begin{bmatrix} \mathcal{L}_{w_x}^{(\beta)} \\ \mathcal{L}_{w_y}^{(\beta)} \end{bmatrix} \begin{Bmatrix} \sum_l^{n_l^{(\beta)}} c_l^{(\beta)} \Psi_l^{(\beta)} \\ \sum_t^{n_t^{(\beta)}} c_t^{(\beta)} \Psi_t^{(\beta)} \end{Bmatrix} + \sum_c^{n_c^{(\beta)}} \begin{Bmatrix} \widehat{w}_{xc} \\ \widehat{w}_{yc} \end{Bmatrix}, \quad (57)$$

with $\Psi_{\bullet}^{(\beta)}$ the wave functions, satisfying the uncoupled Navier equations (3), and $c_{\bullet}^{(\beta)}$ the unknown wave functions contribution factors which are determined by the imposed boundary and interface conditions. The set of wave functions have to form a T-complete set of functions, thereby theoretically ensuring convergence to the exact result [36]. However, when the deformation state becomes singular in a corner point, a prohibitively high number of wave functions is needed to achieve an acceptable prediction accuracy and, because of the ill-conditioning, round-off errors can destroy the accuracy before adequate convergence is achieved [20]. Enrichment of the expansion with some special-purpose functions, that accurately represent the singularity in the deformation state, accelerates the convergence of the WBM significantly. For each corner c of the problem domain in which a singularity is present, the set of wave functions is extended with a set of corner functions $\{\widehat{w}_{xc} \widehat{w}_{yc}\}^T$ whose only purpose is an accurate representation of the singularity in corner c .

4.2.1. Wave functions

Table 2 lists the selected wave functions for subdomain β . The corresponding wavenumbers are defined based on the dimensions $(L_x^{(\beta)} \times L_y^{(\beta)})$ of the preferably smallest rectangular box circumscribing the subdomain, see Fig. 6. Assuming that an integer number of half wavelengths equals the dimension of the rectangular box in the corresponding direction leads to the first wavenumber:

$$k_{l_1,x}^{(\beta)} = \frac{l_1\pi}{L_x^{(\beta)}} \quad \text{and} \quad k_{l_2,y}^{(\beta)} = \frac{l_2\pi}{L_y^{(\beta)}}, \quad (58)$$

for the dilatational field and

$$k_{t_1,x}^{(\beta)} = \frac{t_1\pi}{L_x^{(\beta)}} \quad \text{and} \quad k_{t_2,y}^{(\beta)} = \frac{t_2\pi}{L_y^{(\beta)}}, \quad (59)$$

Table 2. Selected wave functions for subdomain β .

dilatational wave functions	
$\Psi_{l_1}^{(\beta)}(\mathbf{x}) = \sin(k_{l_1,x}^{(\beta)}x) \exp(-jk_{l_1,y}^{(\beta)}y)$	$l_1 = 0, 1, \dots, n_{l_1}^{(\beta)}$
$\Psi_{l_2}^{(\beta)}(\mathbf{x}) = \exp(-jk_{l_2,x}^{(\beta)}x) \sin(k_{l_2,y}^{(\beta)}y)$	$l_2 = 0, 1, \dots, n_{l_2}^{(\beta)}$
$\Psi_{l_1}^{(\beta)}(\mathbf{x}) = \cos(k_{l_1,x}^{(\beta)}x) \exp(-jk_{l_1,y}^{(\beta)}y)$	$l_1 = 1, \dots, n_{l_1}'^{(\beta)}$
$\Psi_{l_2}^{(\beta)}(\mathbf{x}) = \exp(-jk_{l_2,x}^{(\beta)}x) \cos(k_{l_2,y}^{(\beta)}y)$	$l_2 = 1, \dots, n_{l_2}'^{(\beta)}$
rotational wave functions	
$\Psi_{t_1}^{(\beta)}(\mathbf{x}) = \cos(k_{t_1,x}^{(\beta)}x) \exp(-jk_{t_1,y}^{(\beta)}y)$	$t_1 = 0, 1, \dots, n_{t_1}^{(\beta)}$
$\Psi_{t_2}^{(\beta)}(\mathbf{x}) = \exp(-jk_{t_2,x}^{(\beta)}x) \cos(k_{t_2,y}^{(\beta)}y)$	$t_2 = 0, 1, \dots, n_{t_2}^{(\beta)}$
$\Psi_{t_1}^{(\beta)}(\mathbf{x}) = \sin(k_{t_1,x}^{(\beta)}x) \exp(-jk_{t_1,y}^{(\beta)}y)$	$t_1 = 1, \dots, n_{t_1}'^{(\beta)}$
$\Psi_{t_2}^{(\beta)}(\mathbf{x}) = \exp(-jk_{t_2,x}^{(\beta)}x) \sin(k_{t_2,y}^{(\beta)}y)$	$t_2 = 1, \dots, n_{t_2}'^{(\beta)}$

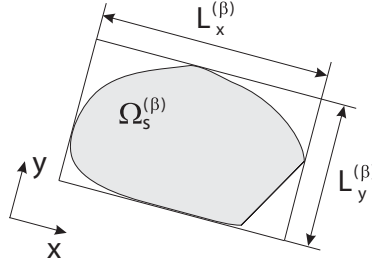


Fig. 6. Definition of the bounding box for subdomain β .

for the rotational field. The other component of the wavenumber is calculated from, respectively, the longitudinal or shear wavenumber associated with the considered frequency:

$$k_{l_1,y}^{(\beta)} = \pm \sqrt{k_l^{(\beta)2} - \left(\frac{l_1\pi}{L_x^{(\beta)}}\right)^2}, \quad k_{l_2,x}^{(\beta)} = \pm \sqrt{k_l^{(\beta)2} - \left(\frac{l_2\pi}{L_y^{(\beta)}}\right)^2}, \quad (60)$$

and

$$k_{t_1,y}^{(\beta)} = \pm \sqrt{k_t^{(\beta)2} - \left(\frac{t_1\pi}{L_x^{(\beta)}}\right)^2}, \quad k_{t_2,x}^{(\beta)} = \pm \sqrt{k_t^{(\beta)2} - \left(\frac{t_2\pi}{L_y^{(\beta)}}\right)^2}. \quad (61)$$

For acoustic problems and plate bending problems, it has been demonstrated that such selection of wave functions leads to convergence provided that the considered subdomain is convex [24, 34]. We assume that this can be extrapolated to problems governed by multiple Helmholtz-equations, as this will be confirmed in the numerical examples in Sec. 5.

The number of wave functions $n_l^{(\beta)} + n_t^{(\beta)}$ that are included in the expansion (57) is related to the excitation frequency and the dimensions of the enclosing rectangular box:

$$n_l^{(\beta)} = 2n_{l_1}^{(\beta)} + 2n_{l_2}^{(\beta)} + 2(n_{l_1}'^{(\beta)} + 1) + 2(n_{l_2}'^{(\beta)} + 1), \quad (62)$$

$$n_t^{(\beta)} = 2(n_{t_1}^{(\beta)} + 1) + 2(n_{t_2}^{(\beta)} + 1) + 2n_{t_1}'^{(\beta)} + 2n_{t_2}'^{(\beta)}, \quad (63)$$

with,

$$\frac{n_{l_1}^{(\beta)}}{L_x^{(\beta)}} \approx \frac{n_{l_2}^{(\beta)}}{L_y^{(\beta)}} \approx \frac{n_{l_1}'^{(\beta)}}{L_x^{(\beta)}} \approx \frac{n_{l_2}'^{(\beta)}}{L_y^{(\beta)}} \approx \frac{n_{t_1}^{(\beta)}}{L_x^{(\beta)}} \approx \frac{n_{t_2}^{(\beta)}}{L_y^{(\beta)}} \approx \frac{n_{t_1}'^{(\beta)}}{L_x^{(\beta)}} \approx \frac{n_{t_2}'^{(\beta)}}{L_y^{(\beta)}} \geq T \frac{k_t}{\pi}, \quad (64)$$

with $n_{\bullet}^{(\beta)}$ integer truncation values and with T a user defined truncation parameter. The truncation rule is based on the in-plane shear wavenumber k_t since it typically exceeds the longitudinal wavenumber k_l and therefore yields the most restricting condition. With this truncation rule, the wavenumbers of the highest oscillating wave functions included in the expansion exceed the in-plane shear wavenumber multiplied with a user defined parameter T .

4.2.2. Corner functions

If stress singularities are present in one or more corners, the expansion of wave functions is extended with a set of corner functions. For each corner c of subdomain β in which singular stresses occur, the following expansion associated with that corner is added to the field variable expansions:

$$\begin{Bmatrix} \widehat{w}_{xc}^{(\beta)} \\ \widehat{w}_{yc}^{(\beta)} \end{Bmatrix} = \begin{bmatrix} \mathcal{L}_{w_x}^{(\beta)} \\ \mathcal{L}_{w_y}^{(\beta)} \end{bmatrix} \begin{Bmatrix} \sum_{l=1}^{n_{cf}} c_{lc} \Upsilon_{lc}^{(\beta)}(r_c, \theta_c) \\ \sum_{t=1}^{n_{cf}} c_{tc} \Upsilon_{tc}^{(\beta)}(r_c, \theta_c) \end{Bmatrix} \quad (65)$$

with $2n_{cf}$ the total number of included corner functions for corner c . The corner functions are multiplied with contribution factors c_{lc} and c_{tc} which are unknowns of the system.

The corner functions are defined as the eigenfunctions of the corresponding infinite wedge domain:

$$\begin{aligned} \Upsilon_{lc}^{(\beta)}(r_c, \theta_c) &= \begin{cases} \cos(\lambda_{lc}\theta_c) J_{\lambda_{lc}}(k_l^{(\beta)} r_c) \\ \sin(\lambda_{lc}^*\theta_c) J_{\lambda_{lc}^*}(k_l^{(\beta)} r_c) \end{cases}, \\ \Upsilon_{tc}^{(\beta)}(r_c, \theta_c) &= \begin{cases} \cos(\lambda_{tc}\theta_c) J_{\lambda_{tc}}(k_t^{(\beta)} r_c) \\ \sin(\lambda_{tc}^*\theta_c) J_{\lambda_{tc}^*}(k_t^{(\beta)} r_c) \end{cases}. \end{aligned} \quad (66)$$

The eigenvalues λ depend on the type of singularity and thus on the boundary conditions along the adjacent edges and the interior angle α_c of the corresponding corner. When both edges are simply supported, the eigenvalues follow from the application of the radial boundary conditions to the dynamic, homogeneous solution of the infinite wedge domain. The eigenvalues are defined as in Eq. (26). For other combinations of boundary conditions, the eigenvalues must be determined from those of the corresponding static problem, as explained in Subsec. 3.5. If the interior angle and radial boundary conditions of the infinite wedge domain correspond with that of the corner in the original problem domain, the eigenfunctions accurately represent the stress singularity in the problem solution.

As indicated in Fig. 7, each corner function is defined in a coordinate system attached to the corresponding corner point. The corner is the origin of the coordinate system and θ is related to the bisecting line. In contrast to the wave functions, which are defined within one subdomain, the corner functions are related to a corner and are not necessarily restricted to one subdomain. In case that the corner point lies on an interface, and thus belongs to several subdomains, the functions associated with that corner extend over the different subdomains adjacent to the corner point. For example, corner c_2 in Fig. 7 belongs to both subdomains $\Omega_s^{(1)}$ and $\Omega_s^{(2)}$. Thus the corner functions associated with this corner extend over the two subdomains. For corner c_1 , on the other hand, the corner functions are only defined inside subdomain $\Omega_s^{(1)}$. Unlike the wave functions, the corner functions do not form a complete set [16]. Therefore, the corner functions can only be used together with the conventional set of wave functions. Since the purpose of the corner functions is merely to give an accurate representation of the singularities in the solution in the vicinity of the corner, only the eigenfunctions that give rise to singularities, i.e., eigenfunctions with an eigenvalue $1 < \lambda < 2$, need to be included in the model.

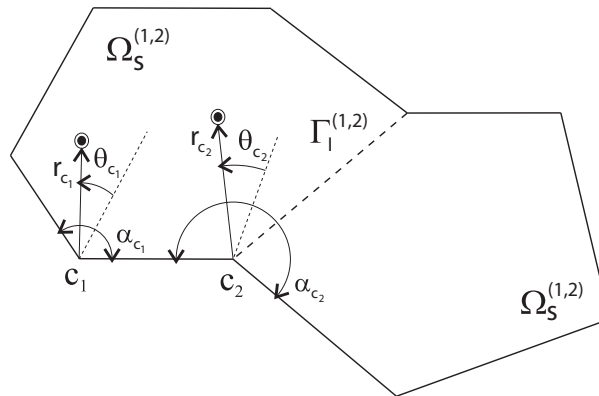


Fig. 7. Definition of corner functions.

4.3. Evaluation of boundary and interface conditions

The field variable expansion (57) satisfies the governing dynamic equations exactly, irrespective of the unknown contribution factors $c_l^{(\beta)}$ and $c_t^{(\beta)}$. The contribution factors are determined through minimisation of the approximation errors of the boundary and interface conditions. Since these conditions are imposed in every point of the subdomain boundary, they can only be satisfied approximately in an integral sense. In this paper, a weighted residual formulation is adopted to enforce the boundary and interface conditions. For each subdomain β , the error residual functions are orthogonalised with respect to some weighting functions $\tilde{e}^{(\beta)}$ and $\tilde{\Omega}^{(\beta)}$ and their derived quantities $\tilde{w}_n^{(\beta)}$, $\tilde{w}_s^{(\beta)}$, $\tilde{T}_n^{(\beta)}$ and $\tilde{T}_s^{(\beta)}$ (cfr. Eq. (9)):

$$\begin{aligned} & \int_{\Gamma_v^{(\beta)} \cup \Gamma_{vt2}^{(\beta)}} \tilde{T}_n^{(\beta)} R_{w_n}^{(\beta)} d\Gamma + \int_{\Gamma_v^{(\beta)} \cup \Gamma_{vt1}^{(\beta)}} \tilde{T}_s^{(\beta)} R_{w_s}^{(\beta)} d\Gamma - \int_{\Gamma_t^{(\beta)} \cup \Gamma_{vt1}^{(\beta)}} \tilde{w}_n^{(\beta)} R_{T_n}^{(\beta)} d\Gamma \\ & - \int_{\Gamma_t^{(\beta)} \cup \Gamma_{vt2}^{(\beta)}} \tilde{w}_s^{(\beta)} R_{T_s}^{(\beta)} d\Gamma + \sum_{\alpha, \alpha \neq \beta} \int_{\Gamma_v^{(\beta, \alpha)}} \left[\tilde{T}_n^{(\beta)} R_{I_{w_n}}^{(\beta, \alpha)} + \tilde{T}_s^{(\beta)} R_{I_{w_s}}^{(\beta, \alpha)} \right] d\Gamma \\ & - \sum_{\alpha, \alpha \neq \beta} \int_{\Gamma_t^{(\beta, \alpha)}} \left[\tilde{w}_n^{(\beta)} R_{IT_n}^{(\beta, \alpha)} + \tilde{w}_s^{(\beta)} R_{IT_s}^{(\beta, \alpha)} \right] d\Gamma = 0. \quad (67) \end{aligned}$$

Like in the Galerkin weighting procedure, the weighting functions $\tilde{e}^{(\beta)}$ and $\tilde{\Omega}^{(\beta)}$ are chosen as an expansion of the same basis functions used for the field variable approximations. Substitution of the field variable approximations and the weighting functions in the weighted residual formulation (67), together with the requirement that these relations should hold for any set of weighting function contribution factors results in a system of equations in the unknown contribution factors. As mentioned before, the corner functions are not necessarily restricted to one subdomain. In the case that a corner function is defined in two subdomains, it will not give rise to an approximation error over the interface between the two subdomains since the continuity is a priori guaranteed. The corner function will therefore be excluded from the residuals over that interface.

For each of the N_s subdomains, a matrix equation in the unknown contribution factors is formulated. Combination of the N_s matrix equations yields the structural WB model.

5. NUMERICAL EXAMPLES

This section demonstrates the computational efficiency of the WBM by means of two cases. The study will confirm the beneficial influence of the corner functions on the achieved prediction accuracy. Furthermore, the performance of the WBM will be compared with that of the FEM. The comparison is made based on both accuracy as well as on computation time. The WB predictions are calculated using a C++ implementation of the WBM. The mentioned computation times for the WBM include both the construction and solution times since the WB models are frequency dependent. As *MSC/Nastran* is a widely accepted tool in the field of structural dynamics, the FE predictions are calculated using *MSC/Nastran*. The considered problems only exhibit a deformation in the plane of the structure, such that the degrees of freedom associated with the out-of-plane deformation can be constrained. The FE models include three degrees of freedom per node. All FE results are calculated with the direct solution method. Computation times only include the direct solution times, such that the times are a measure for the frequency dependent cost. All calculations were performed on a 3 GHz Intel Pentium 4 processor running a Linux operating system.

The first example has a convex problem geometry such that a division in subdomains is not needed. Since no singularities are present in the problem solution, the use of corner functions is

needed neither. The last example consists of a more complex geometry which requires a domain subdivision. In this example, singularities are present. To accelerate the convergence of the WBM, the expansion set is extended with a few corner functions that accurately represent the existing singularities.

5.1. Convex problem without singularities

A first example consists of a convex problem domain as shown in Fig. 8. The material is aluminium ($E = 70 \cdot 10^9 \text{ N/m}^2$, $\nu = 0.3$, $\rho = 2790 \text{ kg/m}^3$) and the structure has a thickness of 0.001 m. A uniform normal force of 1N/m is applied to the upper edge. The bottom edge is fixed, while the two other edges are free. There are two response points located at w_1 (0.25 m, 0.125 m) and w_2 (0.65 m, 0.3 m).

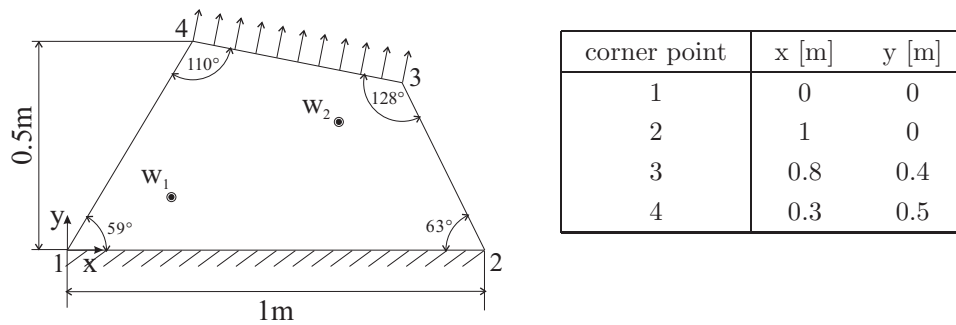


Fig. 8. Geometry of a convex problem without singularities.

Stress singularities

At first, it is verified whether singularities will be present. The combinations of radial boundary conditions appearing in this problem are fixed-free and free-free. For these boundary conditions, no exact dynamic solutions can be defined for the infinite wedge domain. The existing displacement and strain fields are therefore derived from the corresponding static problem. The characteristic equations and critical angles for the static infinite wedge are given in Table 1. For the *fixed-free* infinite wedge, the critical angle equals 60° (for $\nu = 0.3$). As a result singularities may appear in corner 2. The interior angle of this corner lies nevertheless so close to the critical angle that the expected strain and stress gradients are quite small. The smallest eigenvalue for the fixed-free static wedge is $\lambda_s = 0.98$ while the stress fields behave as $r^{\lambda_s - 1}$ around the corner point. Hence, it is expected that the stress gradient will not have a great influence on the performance of the WBM. For a *free-free* corner, singularities exist when the internal angle exceeds 180° so that no singularities are introduced by the homogeneous boundary conditions. However, for corners 3 and 4 the boundary conditions are not homogeneous. The possible singularities include those for the corresponding homogeneous problem as well as those induced by the inhomogeneous conditions. To derive the stress field caused by an applied traction, we consider an infinite wedge domain where the following boundary conditions are applied:

$$\left. \begin{aligned} \sigma_\theta(r, \theta) &= 0 \\ \tau_{r\theta}(r, \theta) &= 0 \end{aligned} \right\} \quad \text{for } \theta = -\frac{\alpha}{2},$$

$$\left. \begin{aligned} \sigma_\theta(r, \theta) &= q \\ \tau_{r\theta}(r, \theta) &= 0 \end{aligned} \right\} \quad \text{for } \theta = \frac{\alpha}{2},$$
(68)

with $0 < r < \infty$. Imposing these boundary conditions to the basic stress fields (29) of a static infinite wedge domain leads to the characteristic system of equations:

$$r^{\lambda_s - 1} \mathbf{A} \mathbf{c} = \mathbf{q},$$
(69)

for $0 < r < \infty$. The coefficient matrix is defined as

$$\mathbf{A} = \lambda_s \begin{bmatrix} C_1 & -S_1 & (\lambda_s + 1)C_2 & -(\lambda_s + 1)S_2 \\ -S_1 & C_1 & -(\lambda_s - 1)S_2 & -(\lambda_s - 1)C_2 \\ C_1 & S_1 & (\lambda_s + 1)C_2 & (\lambda_s + 1)S_2 \\ S_1 & -C_1 & (\lambda_s - 1)S_2 & -(\lambda_s - 1)C_2 \end{bmatrix}, \quad (70)$$

with

$$\begin{aligned} C_1 &= \cos(\lambda_s + 1)\frac{\alpha}{2}, & C_2 &= \cos(\lambda_s - 1)\frac{\alpha}{2}, \\ S_1 &= \sin(\lambda_s + 1)\frac{\alpha}{2}, & S_2 &= \sin(\lambda_s - 1)\frac{\alpha}{2}. \end{aligned} \quad (71)$$

The vectors \mathbf{c} and \mathbf{q} contain, respectively, the integration constants and the applied tractions:

$$\mathbf{c} = \{A_{\lambda_s} \ B_{\lambda_s} \ C_{\lambda_s} \ D_{\lambda_s}\}^T, \quad (72)$$

$$\mathbf{q} = \{0 \ 0 \ q \ 0\}^T. \quad (73)$$

The characteristic equations (69) only hold for all r if $\lambda_s = 1$. Taking into account that for corners 3 and 4 the following relations apply:

$$\cos \alpha \neq 0 \quad \text{and} \quad \sin \alpha \neq 0, \quad (74)$$

yields a system of equations which is only satisfied for the trivial solution. The basic fields that are used to arrive at this solution are incomplete. To overcome this problem, the basic fields are supplemented with the auxiliary fields (45) in accordance with [10]. The characteristic equations are again obtained by applying the boundary conditions to the total stress fields:

$$r^{\lambda_s - 1} \ln r \mathbf{A} \mathbf{c}' + r^{\lambda_s - 1} \left(\mathbf{A} \mathbf{c} + \frac{\partial \mathbf{A}}{\partial \lambda_s} \mathbf{c}' \right) = \mathbf{q}, \quad (75)$$

with \mathbf{c}' the integration constants of the auxiliary fields. Setting $\lambda_s = 1$ makes the second term of the left-hand side independent of the radial coordinate. The first term contains a $\ln r$ term and can only be made independent of r by demanding that its coefficient is zero or

$$\mathbf{A} \mathbf{c}' = \mathbf{0}. \quad (76)$$

This forms no problem since the determinant of \mathbf{A} is zero for $\lambda_s = 1$. Actually, the fact that the determinant of the coefficient matrix is zero prohibited the solution of the inhomogeneous problem with only the basic fields. The solution for the system $\mathbf{A} \mathbf{c}' = \mathbf{0}$ is

$$A'_{\lambda_s} = B'_{\lambda_s} = C'_{\lambda_s} = 0. \quad (77)$$

The constants \mathbf{c} are determined from the remaining conditions taking the solution for \mathbf{c}' and $\lambda_s = 1$ into account:

$$\mathbf{A} \mathbf{c} + \frac{\partial \mathbf{A}}{\partial \lambda_s} \mathbf{c}' = \mathbf{q}. \quad (78)$$

For a corner with internal angle α , the solution is defined as

$$\begin{aligned} D'_{\lambda_s} &= \frac{\cos \alpha}{2(\alpha \cos \alpha - \sin \alpha)} q, \\ A_{\lambda_s} &= 0, \\ B_{\lambda_s} &= -\frac{1}{2(\alpha \cos \alpha - \sin \alpha)} q, \\ C_{\lambda_s} &= \frac{q}{4}. \end{aligned} \quad (79)$$

The corresponding angular stress field becomes

$$\sigma_{\theta} = \frac{2\theta \cos \alpha - \sin 2\theta}{2(\alpha \cos \alpha - \sin \alpha)} q + \frac{q}{2}. \quad (80)$$

The proposed solution clearly satisfies the imposed boundary conditions at $\theta = \pm\alpha/2$. As the solution does not become singular in the corner point, the inhomogeneous boundary conditions caused by the applied tractions do not introduce a singularity in the stress fields. Since the singularities in the stress field for the static and dynamic case are asymptotically identical around the corner point, it can be concluded that the dynamic problem is also free of singularities. Recall that the solution (80) is only valid if the relations

$$\cos \alpha \neq 0 \quad \text{and} \quad \sin \alpha \neq 0 \quad (81)$$

hold. Otherwise it is possible to define the solution for Eq. (69) and the auxiliary fields do not appear in the resulting stress field.

In summary, only in corner 2 a singularity is expected since its interior angle just exceeds the critical angle. The gradient in the stress field will nevertheless remain small such that it does not influence the convergence rate of the WBM.

Computational models

The considered FE models include both a quadrilateral and a triangular discretisation. Only the 4-noded and 3-noded linear elements are used. Both the WB and FE results are compared with a reference solution calculated with a very fine FE model with quadrilateral discretisation. The first FE reference model consists of 366,900 dofs and will be used for the frequency response analysis from 1 to 20 kHz. A second reference model consists of 2,977,089 dofs. This model is the reference model for the convergence analyses at 6, 11.5 and 17.2 kHz. The wavelengths and the number of elements per wavelength of the models at the frequencies of interest are summarised in Table 3.

Table 3. FE reference models.

	frequency [kHz]	λ_{ϵ} [m]	# FE dofs	# elements/ λ_{ϵ}
FRF reference model	1	3.1064	366,900	970
	20	0.1553	366,900	48
Convergence reference model	6	0.5177	2,977,089	431
	11.5	0.2701	2,977,089	225
	17.2	0.1806	2,977,089	150

The analysis considers several WB models which are constructed by applying a different truncation parameter T . The notation “WBM $T \bullet$ ” will be used to indicate that the WBM with a truncation factor \bullet is considered. As explained in Subsubsec. 4.2.1, the number of dofs of the WB models increases with the excitation frequency. Since the problem domain is convex, a subdivision in domains is not required. Since no important stress singularities are present, it is also not necessary to include corner functions.

Response fields

Figure 9 shows the amplitude of the predicted displacement field at 11.5 kHz. The prediction result is calculated with a WB model consisting of 96 dilatational and 96 rotational wave functions, leading to a total of 192 dofs. The figure shows that the fixed boundary conditions at the bottom edge are accurately represented. The accuracy of the WB prediction is displayed in Fig. 10. This figure shows the amplitude of the absolute prediction error as compared to an FE model of 349,173 dofs. The prediction accuracy of the WB model is very good, despite the smaller system matrices. The largest prediction error equals $5.5 \cdot 10^{-11}$ m.

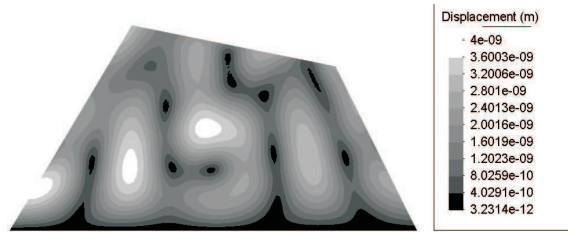


Fig. 9. Amplitude of the forced displacement at 11.5 kHz predicted by the WBM T_2 .

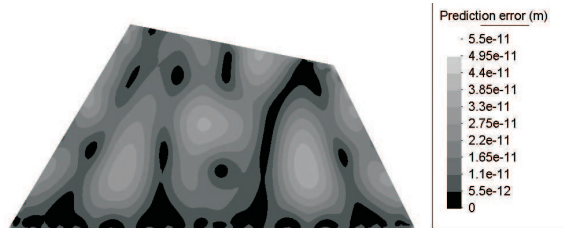


Fig. 10. Amplitude of absolute error on the displacement at 11.5 kHz predicted by the WBM T_2 .

Figures 11, 12 and 13 show, respectively, the predicted stress resultants t_x , t_y and t_{xy} at 11.5 kHz. The figures on the left show the predictions made by the WB model of 192 dofs; the figures on the right show the predictions made by the FE model of 349,173 dofs. The figures indicate that also for the derived secondary variables, there is a good agreement between the FE and WB predictions. For the WBM, the spatial resolution of the derived variables is identical to that of the primary variables. Thus despite the low number of dofs, the accuracy and spatial resolution of the predicted stress resultants are still very good. As discussed before, the interior angles of corners 1 and 2 lie close to the critical value starting from which singularities are induced. The predicted stress resultants show indeed a gradient in the vicinity of these corner points, as opposed to corners 3 and 4. The gradients are nevertheless quite small such that the accuracy of the WBM is hardly affected.

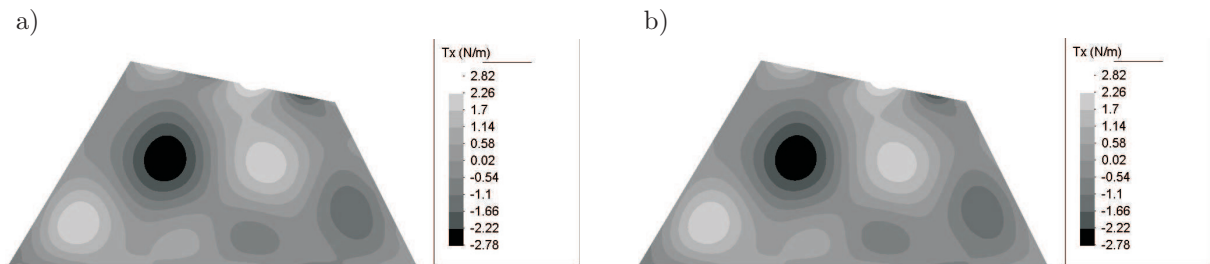


Fig. 11. Predicted in-plane stress resultant t_x at 11.5 kHz: a) WBM T_2 (192 dofs), b) FEM (349,173 dofs).

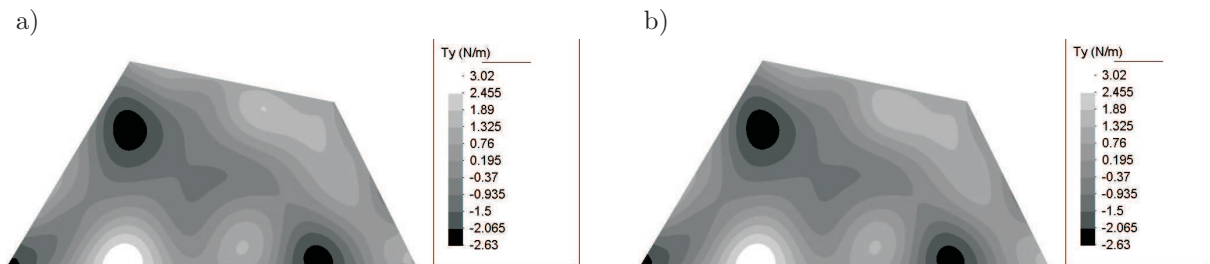


Fig. 12. Predicted in-plane stress resultant t_y at 11.5 kHz: a) WBM T_2 (192 dofs), b) FEM (349,173 dofs).

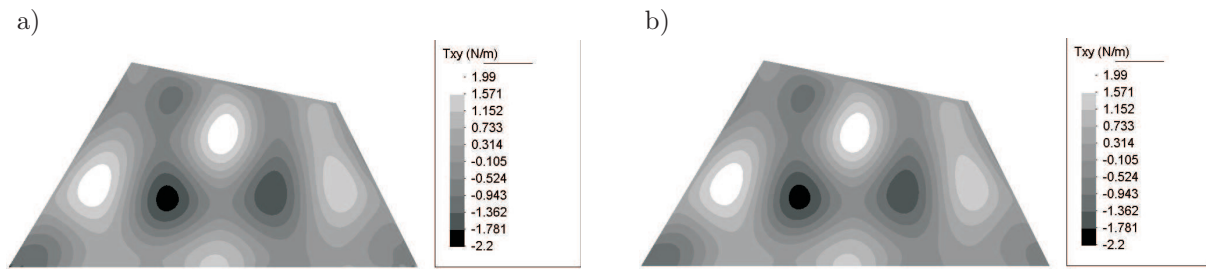


Fig. 13. Predicted in-plane stress resultant t_{xy} at 11.5 kHz: a) WBM T_2 (192 dofs), b) FEM (349,173 dofs).

Convergence analysis

To evaluate the performance of the WBM, a convergence analysis is performed at three different frequencies. The considered frequencies are arbitrarily chosen in the low- and mid-frequency range. The number of structural in-plane modes below the frequencies of interest is given in Table 4. For the convergence analysis, the averaged prediction accuracy of each of the models is plotted as a function of the computation time. The averaged prediction error is defined as the average of the amplitude of the relative prediction error in the $n_{rp} = 2$ response points:

$$\langle \epsilon \rangle = \frac{1}{n_{rp}} \sum_{j=1}^{n_{rp}} \epsilon_j \quad (82)$$

with

$$\epsilon_j = \sqrt{\left(\frac{w_x(\mathbf{x}_j) - w_x^{ref}(\mathbf{x}_j)}{w_x^{ref}(\mathbf{x}_j)} \right)^2 + \left(\frac{w_y(\mathbf{x}_j) - w_y^{ref}(\mathbf{x}_j)}{w_y^{ref}(\mathbf{x}_j)} \right)^2}. \quad (83)$$

As reference solution, the FE model of 2,977,089 dofs is used. See Table 3 for the model details.

Table 4. Number of normal modes below the frequencies considered by the convergence analysis.

frequency [kHz]	# normal modes
6	6
11.5	22
17.2	48

Figure 14 compares the convergence rate of the WBM with that of the FEM. It is seen that the convergence rate of the FEM with quadrilateral discretisation is slightly higher than this of the triangular discretisation. In general, quadrilateral plane elements exhibit a faster convergence, but their performance is more sensitive to distortions of the element shape [26]. Given the moderate geometrical complexity of the considered problem, the better performance of the quadrilateral elements is logical. Furthermore, Fig. 14 shows that the WBM achieves a substantially higher prediction accuracy than the FEM. At 17.2 kHz, the WBM achieves a prediction accuracy of 0.1% after 0.1 CPU seconds, whereas the FEM with quadrilateral discretisation needs almost 1000 CPU seconds to achieve the same accuracy. The WBM achieves a significant increase in computational efficiency as compared to the FEM. However, the figures also show that the accuracy of the WBM stagnates at a certain prediction error. This effect becomes more apparent for higher frequencies. Figure 15 shows the WB convergence curves at 17.2 kHz for three different FE reference models. All three convergence curves show a stagnation, but the stagnation level decreases as the mesh of the FE reference model is refined. Therefore, it is likely that the stagnation of the WB prediction accuracy is not caused by a limitation of the prediction accuracy of the WBM but by the decreasing accuracy of the FE reference model for increasing frequency.

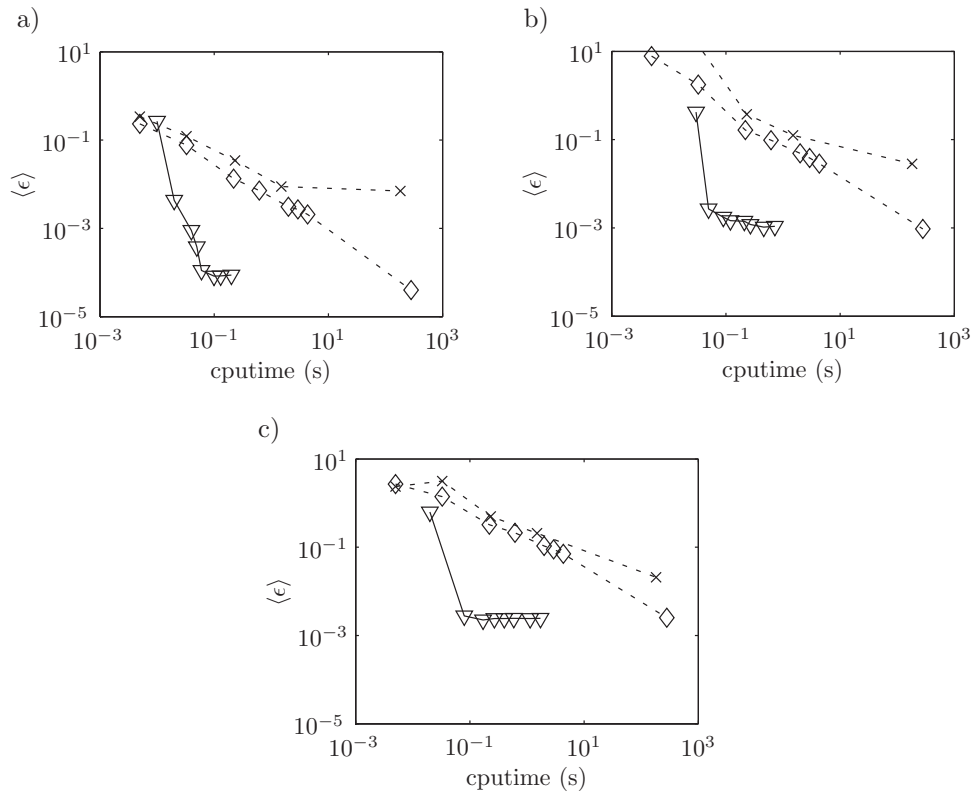


Fig. 14. Comparison of the convergence of the FEM with quadrilateral ($-\diamond-$) and triangular ($-\times-$) discretisations and the WBM ($-\nabla-$): a) 6 kHz, b) 11.5 kHz, c) 17.2 kHz.

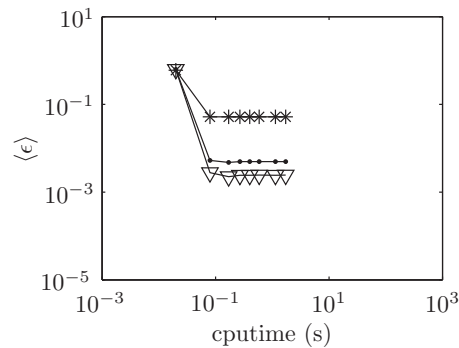


Fig. 15. Influence of the FE reference model on the convergence of the WBM at 17.2 kHz: FE reference of 366,900 dofs ($-\ast-$), 1,458,906 dofs ($-\cdot-$), 2,977,089 dofs ($-\nabla-$).

Frequency response analysis

This section presents the results of a frequency response analysis to compare the performance of the WBM and FEM over a wider frequency range. Figure 16 plots the predicted displacement amplitude for response point w_1 calculated with the FEM and the WBM. Both predictions are compared with an FE reference model consisting of 366,900 dofs (see Table 3). The figure on the top gives the prediction made by the reference model and the WB model. The WB model is constructed using a truncation parameter $T = 1$. Figure 17 shows how the total number of wave functions increases with frequency. Half of the wave functions are used to approximate the dilatational strain and the other half to approximate the rotational strain. The computation time as a function of the excitation frequency is shown in Fig. 18. The main part of the computation time is spent in building the frequency dependent model. The model construction time is shown in Fig. 18a. The time required for the remaining frequency dependent tasks, such as creation of wave functions, model solution and post-processing of the results, is shown in Fig. 18b. In total

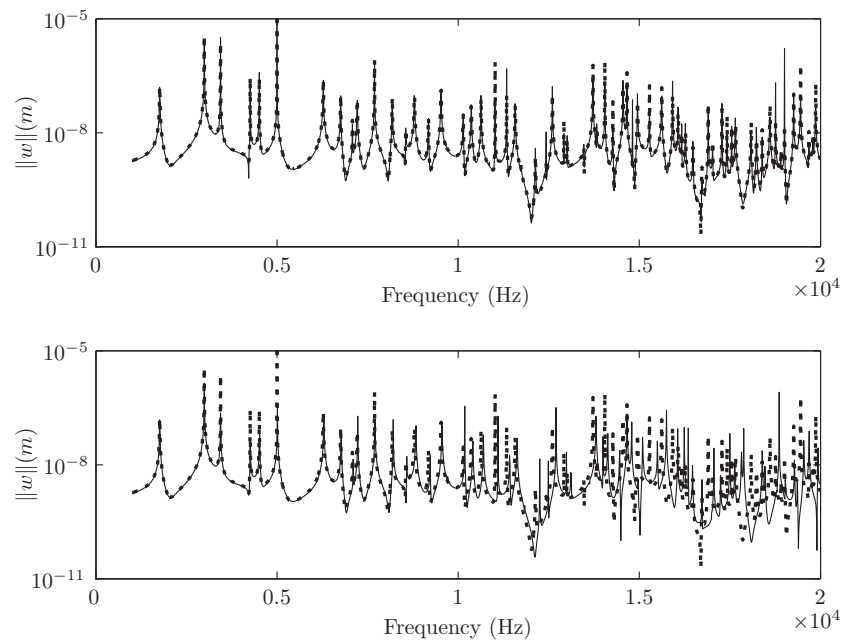


Fig. 16. Frequency response function for response point w_1 (dashed: FE reference 366,900 dofs; solid: WBM $T1$ (top) or FEM 3,774 dofs – 4elements/ λ_b (bottom)). The WBM $T1$ and FEM of 3,774 dofs have a comparable computational load.

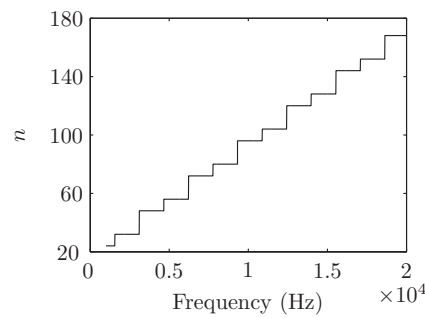


Fig. 17. Number of wave functions for the WBM with $T = 1$.

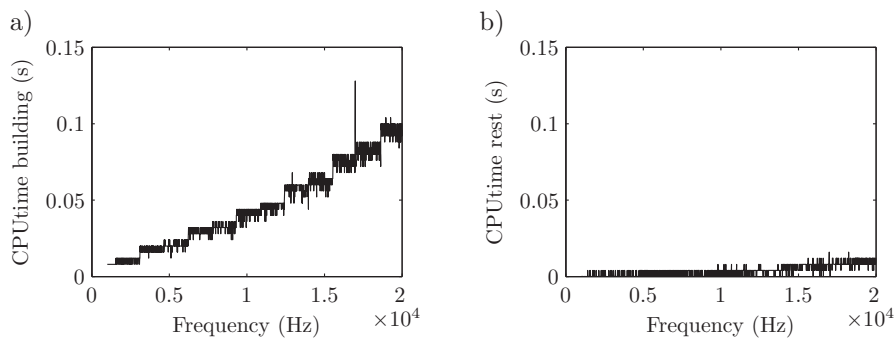


Fig. 18. Frequency dependent computation time for the WBM with $T = 1$: a) cpu time for model construction, b) cpu time for remaining tasks.

the WB model needs 95 CPU seconds to calculate the entire frequency response function, which consists of 1,900 frequency lines. As indicated in Fig. 16, the WB prediction corresponds very well with the reference result over the entire frequency range. The FE model, whose result is shown in the bottom figure, consists of 3,774 dofs and the largest element size is 0.034 m (4 elements/ λ_b). The FE model needs approximately the same computation time as the WB model to calculate

the frequency response function, i.e. 93 CPU seconds. The FE prediction is only accurate in the low-frequency range. Starting from 1 kHz the FE prediction suffers from dispersion errors which result in a frequency shift compared to the reference results. Especially for the higher frequencies, the WB model achieves a substantially higher prediction accuracy compared to the FE model, even though both require the same computational load. The frequency response analysis confirms the results of the convergence analysis, namely that the WBM is capable of predicting more accurate results with a smaller computational load, especially for increasing frequency.

5.2. L-shape

The second example considers a non-convex problem geometry such that a division in subdomains becomes necessary. It consists of an aluminium, L-shaped structure with a thickness of $h = 0.002$ m ($E = 70 \cdot 10^9$ N/m², $\nu = 0.3$, $\rho = 2790$ kg/m³). The location of the corner points is given in Table 5. As indicated in Fig. 19 two edges are fixed, while the other edges are free. Along one of the edges, a normal in-plane force of 1 N/m is applied. There are eight response points whose coordinates are listed in Table 6.

Table 5. Corner points of the L-shape.

corner point	x [m]	y [m]
1	0	0
2	1	0
3	1	-0.5
4	1.5	-0.5
5	1.5	0.5
6	0	0.5

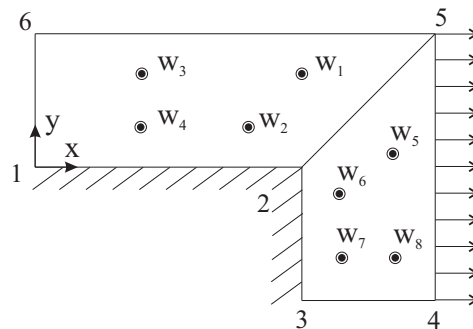


Fig. 19. L-shaped problem geometry.

Table 6. Response points for the L-shape.

response point	x [m]	y [m]
w_1	1	0.35
w_2	0.8	0.15
w_3	0.4	0.35
w_4	0.4	0.15
w_5	1.35	0.05
w_6	1.15	-0.1
w_7	1.15	-0.34
w_8	1.35	-0.34

Stress singularities

Three combinations of boundary conditions occur in this problem, i.e., fixed-fixed, free-free and fixed-free. For each of these combinations it is impossible to define an analytical solution for the dynamic infinite wedge problem. The singularities must be classified starting from the solutions of the corresponding static problem (see Table 1). Consider first the stress field resulting from the homogeneous boundary conditions. For free-free and fixed-fixed corners, singularities appear if the internal angle exceeds 180° . Hence, singularities can be expected in corner 2 ($\alpha = 270^\circ$) for which both radial edges are fixed. The characteristic equation for a fixed-fixed infinite wedge corresponds with

$$\sin \lambda_s \alpha = \pm \lambda_s \frac{1 + \nu}{3 - \nu} \sin \alpha. \quad (84)$$

To determine the static eigenvalues, this nonlinear system of equations must be solved. Since this solution cannot be performed analytically, the system of equations is solved numerically in *Matlab*. The used algorithm is based on the trust-region dogleg method, which is a variant of the Powell's dogleg method [25]. The solution of the system is calculated for a large number of start values to obtain all possible solutions. Solution of the system of equations leads to the static eigenvalues:

$$\begin{aligned} \lambda_{s1,2} &= 0.6040, \\ \lambda_{s2,2} &= 0.7445, \end{aligned} \quad (85)$$

for an infinite wedge of 270° . No logarithmic stress fields are present in the solution since the rank of the coefficient matrix equals its order for each of the eigenvalues. Substitution of the static eigenvalues in the system of equations resulting from the application of boundary conditions, shows that the eigenvalue $\lambda_{s1,2}$ induces an anti-symmetric radial displacement field w_r and a symmetric angular displacement field w_θ . The second eigenvalue $\lambda_{s2,2}$ provokes a symmetric radial and anti-symmetric angular displacement field. Since only power singularities appear in the static stress fields, the dynamic eigenvalues can be chosen to yield asymptotically the same singular behaviour in the dynamic stress fields:

$$\begin{aligned} \lambda_{t1,2}^* &= \lambda_{t1,2} = \lambda_{s1,2} + 1, \\ \lambda_{t1,2} &= \lambda_{t1,2}^* = \lambda_{s2,2} + 1. \end{aligned} \quad (86)$$

For a fixed-free infinite wedge the critical angle is 60° . Corners 1 and 3 have an internal angle of 90° such that also here singularities can be expected. The corresponding characteristic equation is given in Table 1. For an internal angle of 90° the static eigenvalues which induce a singularity are

$$\lambda_{s1,1} = 0.7583 \quad \text{and} \quad \lambda_{s1,3} = 0.7583. \quad (87)$$

The resulting displacement fields include both a symmetric and anti-symmetric component. Also in this case, no auxiliary fields participate in the solution such that the dynamic solution is asymptotically equivalent in the vicinity of the corner point if

$$\lambda_{t1,\bullet} = \lambda_{t1,\bullet}^* = \lambda_{t1,\bullet} = \lambda_{s1,\bullet} + 1, \quad (88)$$

where \bullet corresponds to the considered corner 1 or 3.

The resulting stress fields must be extended with the stress fields induced by the inhomogeneous boundary conditions. For corners 4 and 5 a non-zero traction is applied along one radial edge, while the other edge is free of tractions. Determination of this stress field is performed in a similar way as for the first example taking into account that in this case $\cos \alpha = 0$. The resulting integration constants:

$$A_{\lambda_s} = 0, \quad B_{\lambda_s} = \frac{q}{2} \quad \text{and} \quad C_{\lambda_s} = \frac{q}{4} \quad (89)$$

with q the applied boundary traction, lead to the following stress field:

$$\sigma_\theta = \frac{q}{2} \sin 2\theta + \frac{q}{2}. \quad (90)$$

The stress field does not exhibit a singularity in the corner point and will therefore not be taken into account in the dynamic solution.

In conclusion, stress singularities can appear in corners 1, 2 and 3. The corner functions which correctly represent the singular behaviour in the vicinity of these corner points are summarised in Table 7.

Table 7. Eigenfunctions and eigenvalues for the L-shaped problem.

corner	angle	eigenfunction	eigenvalue
1	90°	$\Upsilon_{l1,1} = \cos(\lambda_{l1,1}\theta)J_{\lambda_{l1,1}}(k_l r)$	$\lambda_{l1,1} = 1.7583$
		$\Upsilon_{l2,1} = \sin(\lambda_{l1,1}^*\theta)J_{\lambda_{l1,1}^*}(k_l r)$	$\lambda_{l1,1}^* = 1.7583$
		$\Upsilon_{t1,1} = \cos(\lambda_{t1,1}\theta)J_{\lambda_{t1,1}}(k_t r)$	$\lambda_{t1,1} = 1.7583$
		$\Upsilon_{t2,1} = \sin(\lambda_{t1,1}^*\theta)J_{\lambda_{t1,1}^*}(k_t r)$	$\lambda_{t1,1}^* = 1.7583$
2	270°	$\Upsilon_{l1,2} = \cos(\lambda_{l1,2}\theta)J_{\lambda_{l1,2}}(k_l r)$	$\lambda_{l1,2} = 1.7445$
		$\Upsilon_{l2,2} = \sin(\lambda_{l1,2}^*\theta)J_{\lambda_{l1,2}^*}(k_l r)$	$\lambda_{l1,2}^* = 1.6040$
		$\Upsilon_{t1,2} = \cos(\lambda_{t1,2}\theta)J_{\lambda_{t1,2}}(k_t r)$	$\lambda_{t1,2} = 1.6040$
		$\Upsilon_{t2,2} = \sin(\lambda_{t1,2}^*\theta)J_{\lambda_{t1,2}^*}(k_t r)$	$\lambda_{t1,2}^* = 1.7445$
3	90°	$\Upsilon_{l1,3} = \cos(\lambda_{l1,3}\theta)J_{\lambda_{l1,3}}(k_l r)$	$\lambda_{l1,3} = 1.7583$
		$\Upsilon_{l2,3} = \sin(\lambda_{l1,3}^*\theta)J_{\lambda_{l1,3}^*}(k_l r)$	$\lambda_{l1,3}^* = 1.7583$
		$\Upsilon_{t1,3} = \cos(\lambda_{t1,3}\theta)J_{\lambda_{t1,3}}(k_t r)$	$\lambda_{t1,3} = 1.7583$
		$\Upsilon_{t2,3} = \sin(\lambda_{t1,3}^*\theta)J_{\lambda_{t1,3}^*}(k_t r)$	$\lambda_{t1,3}^* = 1.7583$

Computational models

The analysis only considers FE models consisting of a linear 4-noded discretisation. As reference solution, a very fine FE model is used. The reference model for the frequency response analysis consists of 121,503 dofs, whereas the reference model for the convergence analysis consists of 3,007,503 dofs. Table 8 gives the details of both reference models.

Table 8. FE reference models.

frequency [kHz]	λ_t [m]	# FE dofs	# elements/ λ_t
0.5	6.2128	121,503	887
15	0.2071	121,503	29
2.5	1.2426	3,007,503	887
9	0.3451	3,007,503	246
15.1	0.2057	3,007,503	146

Since the problem domain is non-convex, the WBM requires a subdivision in domains for convergence reasons. As shown in Fig. 19, the problem domain is divided in two subdomains. Stress singularities are expected to occur such that also WB models with corner functions are considered. The models that include the corner functions listed in Table 7, are indicated by *CF*.

Response fields

A first evaluation of the prediction accuracy of the WBM is based on the predicted response fields. The amplitude of the predicted displacement field at 9 kHz is shown in Fig. 20. The WB model



Fig. 20. Amplitude of the forced displacement at 9 kHz predicted by the WBM *CF T2*.

consists of 200 wave functions for the first subdomain, 152 wave functions for the second subdomain and 12 corner functions, leading to a total of 364 dofs. The figure shows that the boundary and interface conditions on the displacement field are accurately represented. The amplitude of the absolute prediction error of the WB result is shown in Fig. 21; the FE model of 121,503 dofs is used as reference. Despite the smaller system matrices of the WBM, its prediction accuracy is very good.

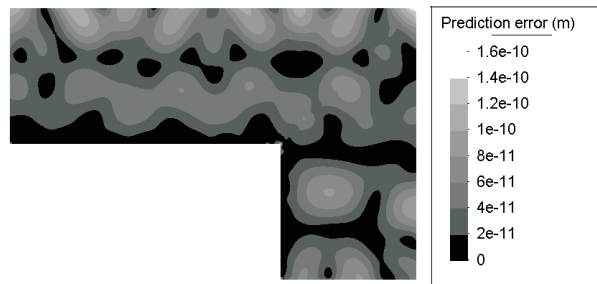


Fig. 21. Amplitude of absolute error of the displacement at 9 kHz predicted by the WBM *CF T2*.

Figure 22 shows the predicted stress resultant t_x at 9 kHz. The prediction is made by the WB model described in the previous paragraph. It is seen that in corners 2 and 3 the stress resultant exhibits a large gradient, indicating that the stress fields become singular in these corners. In corner 1 the stress resultant t_x does not exhibit a strong gradient at the considered frequency. Figure 23 plots the predicted stress resultant t_x as a function of the x -coordinate along the line $y = 0$. For $x = 1.5$ m, the stress resultant equals 1 N/m, which corresponds with the applied boundary force along that edge. As demonstrated by the previous figure, the stress resultant does not exhibit a strong gradient in corner 1 ($x = 0$ m). In corner 2 ($x = 1$ m), the gradient is much more pronounced. Thanks to the included corner functions, the WBM is capable of representing the singularities and associated gradients in the actual stress field accurately. Since the solution expansion of the FEM only consists of polynomial functions, the stresses predicted by the FEM are inaccurate in a small region near the edge, even when a fine discretisation is used.



Fig. 22. In-plane stress resultant t_x at 9 kHz predicted by the WBM *CF T2*.

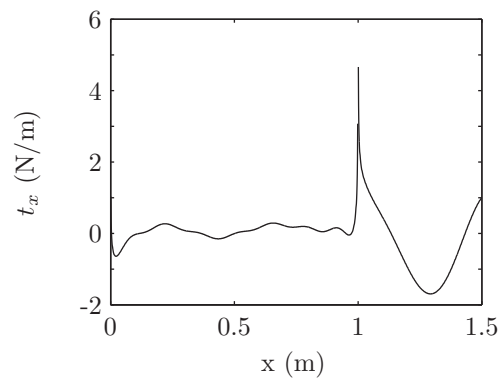


Fig. 23. In-plane stress resultant t_x along the line $y = 0$ at 9 kHz predicted by the WBM *CF T2*.

Convergence analysis

The performance of the WBM is evaluated by a convergence analysis at the frequencies 2.5, 9 and 15.1 kHz. The number of structural in-plane modes below the frequencies of interest are given in Table 9. Figure 24 plots the averaged prediction error defined in Eq. (82) as a function of the

Table 9. Number of normal modes below the frequencies considered by the convergence analysis.

frequency [kHz]	# normal modes
2.5	5
9.0	43
15.1	113

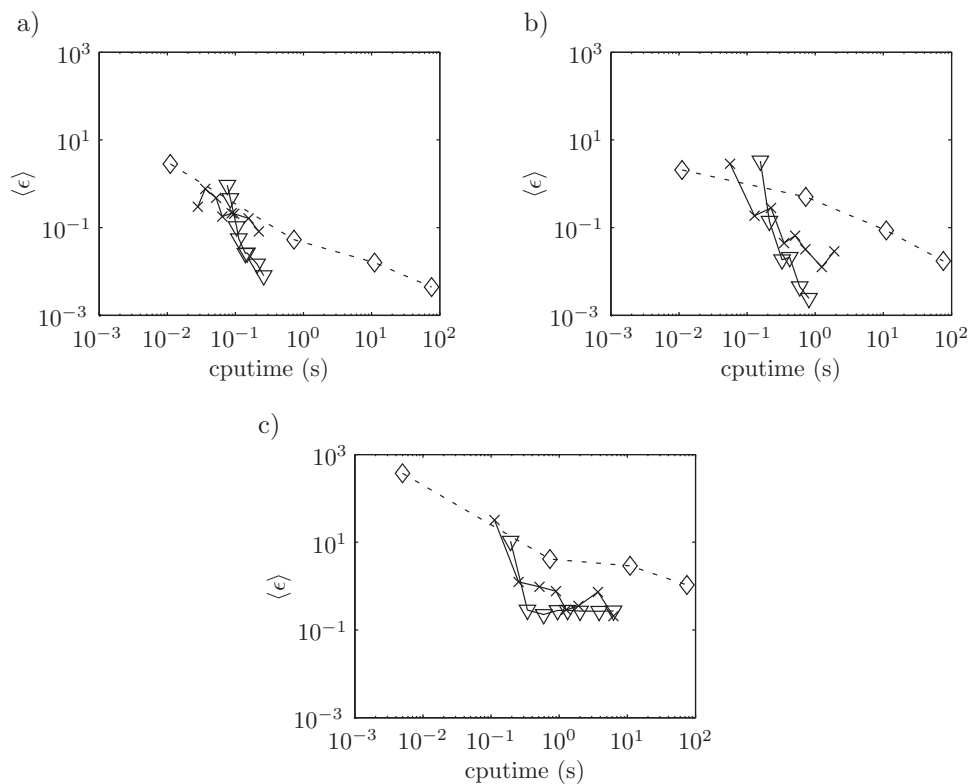


Fig. 24. Comparison of the convergence of the FEM ($-\diamond-$), the WBM ($-\times-$) and the WBM *CF* ($-\nabla-$): a) 2.5 kHz, b) 9 kHz, c) 15.1 kHz.

computation time for the three frequencies. As reference solution the FE model with 3,007,503 dofs is used. The details of this model can be found in Table 8. First, the figure indicates that the inclusion of corner functions accelerates the convergence of the WBM. Compared with the FEM, the WBM CF exhibits a substantially higher convergence rate. However, the WB convergence curve at 15.1 kHz shows a stagnation. This phenomenon also appeared for the previous example. It is likely that the stagnation of the convergence curves is caused by the decreasing accuracy of the reference model.

Frequency response analysis

A frequency response analysis allows to compare the results of the WBM and FEM for a frequency range rather than at discrete frequencies. Figures 25 and 26 plot the displacement amplitude for response point w_1 in the low- and mid-frequency region, respectively. The predictions made by the WBM and FEM are compared with the result of the FE reference model of 121,503 dofs. Table 8 lists some model details. The figures on the top give the prediction made by the reference and WB model. The WB model is built with a truncation parameter $T = 1$. Figure 27 displays the number of WB dofs as a function of frequency. The computation time is shown in Fig. 28. Only the construction and solution times are included since the time required for the remaining tasks is negligible. The major part of the computation time is dedicated to the construction of the WB model. In total the WBM needs 288 CPU seconds to calculate the frequency response function. The bottom figure shows the predictions made by the FEM and the reference model. The FE model consists of 19,833 dofs. The largest element size equals 0.027 m, where the shear wavelength at 15 kHz is 0.2071 m (7 elements/ λ_t). It takes the FE model 500 CPU seconds to calculate the frequency response function. For the low-frequency range, indicated in Fig. 25, both the results of the FEM and WBM correspond very well with the reference solution. However, starting from approximately 6 kHz the FE prediction starts to deteriorate. Figure 26 shows the predictions in the mid-frequency range. Also in this frequency range, the WB results correspond very well with the reference solution. The accuracy of the coarse FE result is however rather poor. Hence, for the mid-frequency range the WBM achieves a substantially higher prediction accuracy compared to the FEM, despite the lower computation time of the WBM.

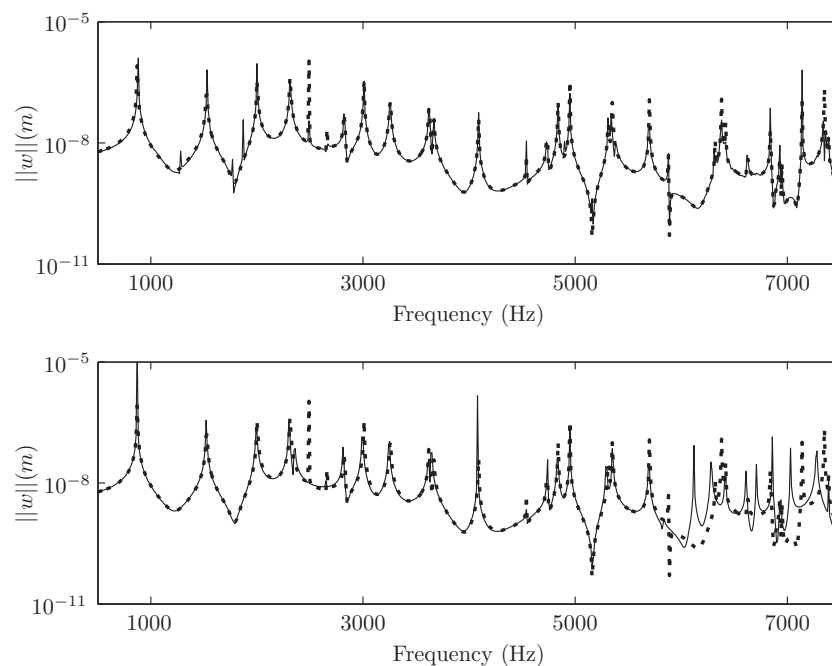


Fig. 25. Frequency response function for response point w_1 (dashed: FE reference 121,503dofs; solid: WBM $CF T1$ (top) or FEM 19,833 dofs – 7elements/ λ_t (bottom)). The WBM $CF T1$ and FEM of 19,833 dofs have a comparable computational load.

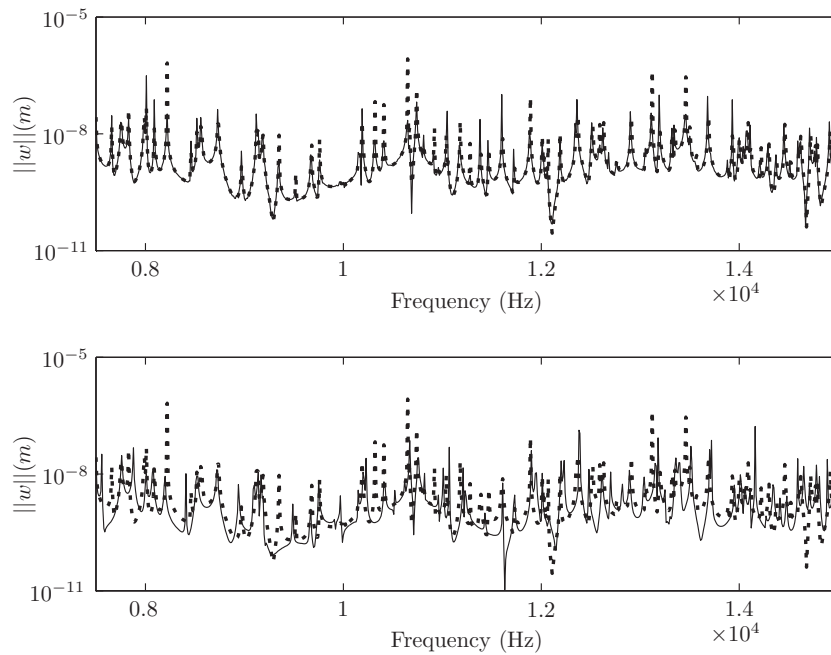


Fig. 26. Frequency response function for response point w_1 in the mid-frequency range (dashed: FE reference 121,503dofs; solid: WBM $CF\ T1$ (top) or FEM 19,833 dofs – 7elements/ λ_t (bottom)). The WBM $CF\ T1$ and FEM of 19,833 dofs have a comparable computational load.

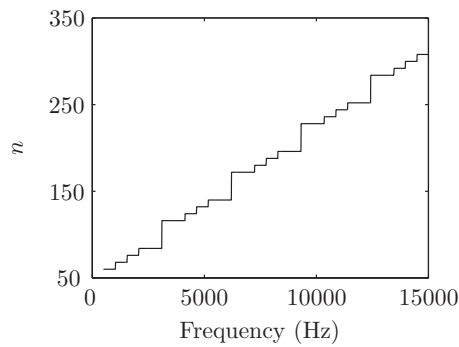


Fig. 27. Number of dofs for the WBM CF with $T = 1$.

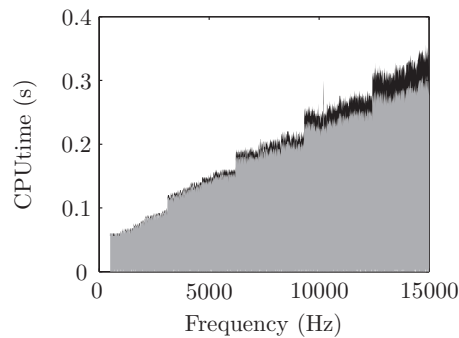


Fig. 28. Frequency dependent computation time for the WBM CF with $T = 1$ (building model (grey), solving model (black)).

Finally, the influence of the corner functions is shown in Fig. 29. This figure plots the displacement amplitude predicted with the WBM with and without corner functions. The truncation parameter is $T = 1$ for both models. Except for the 12 corner functions, the models are identical.

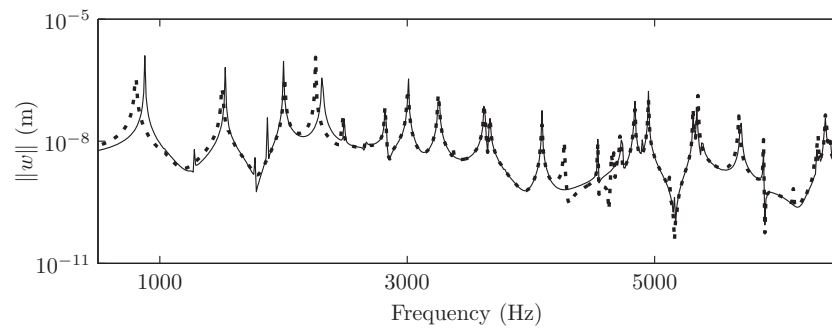


Fig. 29. Frequency response function for response point w_1 (dashed: WBM; solid: WBM CF).

As can be seen in Fig. 29, there is a substantial difference between both prediction results. The corner functions clearly improve the prediction accuracy of the WBM.

6. CONCLUSIONS

This paper extends the application range of the novel WBM to the prediction of the in-plane behaviour of 2D structural solid problems. The basic principles of the WBM are similar to those for plate bending problems [34]. The field variables are approximated by an expansion that satisfies the governing dynamic equations *a priori*. The only approximation errors are induced in the boundary and interface conditions. Minimisation of these errors leads to the solution of the system. Special attention is paid to problems in which stress singularities occur. For a polygonal domain, stress singularities can appear in a corner point if the interior angle of the corner exceeds a critical value. The critical value depends on the type of boundary conditions applied along the edges adjacent to the corner. In case that singularities appear in the problem solution, the conventional set of wave functions is extended with some corner functions that are capable of representing the singularity correctly. An asymptotic analysis of the infinite wedge domain allows to define the appropriate corner functions. In some specific configurations, logarithmic singularities appear. Currently, no dynamic solution has been defined that is capable of representing the logarithmic singularity accurately. To guarantee the general applicability of the WBM, the influence of these singularities on the performance of the WBM should be evaluated. And if necessary, the appropriate corner functions must be defined.

The capabilities of the WBM are demonstrated through two numerical examples. Both examples indicate that the proposed WBM achieves accurate results. Extension of the expansion set with a few corner functions for each corner in which singularities occur, accelerates the convergence of the WBM significantly in case of stress singularities. Furthermore the performance of the WBM has been compared with that of the FEM, where both a quadrilateral and triangular discretisations are considered. The WBM exhibits a substantially increased convergence rate over the FEM. Consequently, the WBM is capable of making accurate predictions up to a higher frequency than the FEM for the same computational load, which indicates the potential of the WBM as an efficient mid-frequency prediction technique.

ACKNOWLEDGMENTS

The research work of Caroline Vanmaele was financed by a scholarship of the Institute for the Promotion of Innovation through Science and Technology in Flanders (IWT-Vlaanderen).

The research work of Karel Vergote was financed by a scholarship of the Fund for Scientific Research – Flanders (FWO-Vlaanderen).

REFERENCES

- [1] M. Abramowitz, I.A. Stegun. Handbook of Mathematical Functions. Dover Publications, New York, 1970.
- [2] J.D. Achenbach. Wave propagation in elastic solids, 6th. North-Holland, Amsterdam, 1990.
- [3] N.S. Bardell, R.S. Langley, J.M. Dunsdon. On the free in-plane vibration of isotropic plates. *Journal of Sound and Vibration*, **191**: 459–467, 1996.
- [4] K.J. Bathe, E.L. Wilson. Numerical methods in finite element analysis. Prentice-Hall Inc., New Jersey, 1976.
- [5] B. Bergen, B. Van Genechten, D. Vandepitte, W. Desmet. An efficient Trefftz-based method for three-dimensional Helmholtz problems in unbounded domains. *Computer Modeling in Engineering and Structures*, **61**: 155–175, 2010.
- [6] L. Blanc, C. Blanzé, P. Rouch. A multiscale “Trefftz” computational method for medium-frequency vibrations of assemblies of heterogeneous plates with uncertainties. *Computers & Structures*, **85**: 595–605, 2007.
- [7] D.B. Bogy. On the problem of edge-bonded elastic quarter-planes loaded at the boundary. *International Journal of Solids and Structures*, **6**: 1287–1313, 1970.
- [8] E. Deckers, D. Vandepitte, W. Desmet. Efficient treatment of stress singularities in poroelastic Wave Based models using special purpose enrichment functions. *Computers & Structures*, **89**: 1117–1130, 2011.
- [9] E. Deckers, N.-E. Hörlin, D. Vandepitte, W. Desmet. A Wave Based Method for the efficient solution of the 2D poroelastic Biot equations. *Computer Methods in Applied Mechanics and Engineering*, **201–204**: 245–262, 2012.
- [10] J.P. Dempsey. The wedge subjected to tractions: A paradox resolved. *Journal of Elasticity*, **11**: 1–10, 1981.
- [11] J.P. Dempsey. Power-logarithmic stress singularities at bi-material corners and interface cracks. *Journal of Adhesion Science and Technology*, **9**: 253–265, 1995.
- [12] W. Desmet. A Wave based prediction technique for coupled vibro-acoustic analysis. Ph.D. Dissertation, Katholieke Universiteit Leuven, Departement Werktuigkunde, Leuven, 1998 (http://www.mech.kuleuven.be/mod/wbm/phd_dissertations).
- [13] G. Fairweather, A. Karageorghis. The method of fundamental solutions for elliptic boundary value problems. *Advances in Computational Mathematics*, **9**: 69–95, 1998.
- [14] D.J. Gorman. Exact solutions for the free in-plane vibration of rectangular plates with two opposite edges simply-supported. *Journal of Sound and Vibration*, **294**: 131–161, 2006.
- [15] J. Jirousek, A. Wróblewski. T-elements: state-of-the-art and future trends. *Archives of Computational Methods in Engineering*, **3**: 323–434, 1996.
- [16] C.S. Huang. Singularities in plate vibration problems. Ph.D. dissertation, The Ohio State University, 1991.
- [17] J.K. Knowles, T.A. Pucik. Uniqueness for plane crack problems in linear elastostatics. *Journal of Elasticity*, **3**: 155–160, 1973.
- [18] P. Ladevèze. A new computational approach for structure vibrations in the medium frequency range. *Compte rendu de l’académie des sciences de Paris, Série IIb*, **332**: 849–946, 1996.
- [19] A. Leissa, O.G. McGee, C.S. Huang. Vibrations of Sectorial Plates having Corner Stress Singularities. *Journal of Applied Mechanics*, **60**: 134–140, 1993.
- [20] A.W. Leissa. Singularity considerations in membrane, plate and shell behaviors. *International Journal of Solids and Structures*, **38**: 3341–3353, 2001.
- [21] R.H. MacNeal. Finite Elements: their design and performance. Marcel Dekker Inc, New York, 1994.
- [22] B. Pluymers, W. Desmet, D. Vandepitte, P. Sas. On the use of a wave based prediction technique for steady-state structural-acoustic radiation analysis. *Journal of Computer Modeling in Engineering & Sciences*, **7**: 173–184, 2005.
- [23] B. Pluymers, C. Vanmaele, W. Desmet, D. Vandepitte. Application of a hybrid finite element – Trefftz approach for acoustic analysis. *Computer Assisted Mechanics and Engineering Sciences*, **13**: 427–444, 2006.
- [24] B. Pluymers, B. Van Hal, D. Vandepitte, W. Desmet. Trefftz-based methods for time-harmonic acoustics. *Archives of Computational Methods in Engineering*, **14**: 343–381, 2007.
- [25] M.J.D. Powell. A Fortran Subroutine for Solving Systems of Nonlinear Algebraic Equations. In: P. Rabinowitz ed., Numerical Methods for Nonlinear Algebraic Equations, Ch.7. 1970.
- [26] J. Robinson. An evaluation of skew sensitivity of thirty three plate bending elements in nineteen FEM systems. Finite Element News – special report (1985).
- [27] A. Seweryn, K. Molski. Elastic stress singularities and corresponding generalized stress intensity factors for angular corners under various boundary conditions. *Engineering Fracture Mechanics*, **55**: 529–556, 1996.
- [28] G.B. Sinclair. Stress singularities in classical elasticity – I: Removal, interpretation and analysis. *Applied Mechanics Reviews*, **57**: 251–297, 2004.
- [29] G.B. Sinclair. Stress singularities in classical elasticity – II: Asymptotic identification. *Applied Mechanics Reviews*, **57**: 385–439, 2004.
- [30] G.B. Sinclair. Logarithmic stress singularities resulting from various boundary conditions in angular corners of plates in extension. *ASME Journal of Applied Mechanics*, **66**: 556–560, 1999.
- [31] P. Tong, T.H.H. Pian. On the convergence of the finite element method for problems with singularity. *International Journal of Solids and Structures*, **9**: 313–321, 1972.

-
- [32] E. Trefftz. Ein Gegenstück zum Ritschen Verfahren. In: Proceedings of the 2nd International Congress on Applied Mechanics, 131–137. Zürich, Switzerland, 1926.
- [33] B. Van Hal, W. Desmet, D. Vandepitte. Hybrid finite element - wave based method for steady-state interior structural-acoustic problems. *Computers & Structures*, **83**: 167–180, 2005.
- [34] C. Vanmaele, D. Vandepitte, W. Desmet. An efficient Wave Based prediction technique for plate bending vibrations. *Computer Methods in Applied Mechanics and Engineering*, **196**: 3178–3189, 2007.
- [35] C. Vanmaele, D. Vandepitte, W. Desmet. An efficient wave based prediction technique for dynamic plate bending problems with corner stress singularities. *Computer Methods in Applied Mechanics and Engineering*, **198**: 2227–2245, 2009.
- [36] C. Vanmaele. Development of a wave based prediction technique for the efficient analysis of low- and mid-frequency structural vibrations. Ph.D. dissertation, Katholieke Universiteit Leuven, Departement Werktuigkunde, Leuven, 2007 (http://www.mech.kuleuven.be/mod/wbm/phd_dissertations).
- [37] B. Van Genechten, D. Vandepitte, W. Desmet. A direct hybrid finite element – wave based modelling technique for efficient coupled vibro-acoustic analysis. *Computer Methods in Applied Mechanics and Engineering*, **200**: 742–746, 2011.
- [38] K. Vergote, B. Van Genechten, D. Vandepitte, W. Desmet. On the analysis of vibro-acoustic systems in the mid-frequency range using a hybrid deterministic-statistical approach. *Computers & Structures*, **89**: 868–877, 2011.
- [39] M.L. Williams. Stress Singularities Resulting from various Boundary Conditions in Angular Corners of Plates in Extension. *Journal of Applied Mechanics*, **74**: 526–528, 1952.
- [40] O.C. Zienkiewicz, R.L. Taylor, J.Z. Zhu, P. Nithiarasu. The Finite Element Method – The three volume set. Butterworth-Heinemann, 2005.